HAL
open science

Experimental Study of the Cr-Hf-Nb System: Liquidus Projection and 1200 °C Isothermal Section

João Carlos Jânio Gigolotti, Antonio Augusto Araújo Pinto da Silva, Gilberto Carvalho Coelho, Carlos Angelo Nunes, Jean-Marc Joubert

▶ **To cite this version:**

João Carlos Jânio Gigolotti, Antonio Augusto Araújo Pinto da Silva, Gilberto Carvalho Coelho, Carlos Angelo Nunes, Jean-Marc Joubert. Experimental Study of the Cr-Hf-Nb System: Liquidus Projection and 1200 °C Isothermal Section. Journal of Phase Equilibria and Diffusion, 2020, 41 (5), pp.702-721. 10.1007/s11669-020-00838-w . hal-03030400

HAL Id: hal-03030400

https://hal.science/hal-03030400v1

Submitted on 1 Dec 2020

HAL is a multi-disciplinary open access archive for the deposit and dissemination of scientific research documents, whether they are published or not. The documents may come from teaching and research institutions in France or abroad, or from public or private research centers.

L'archive ouverte pluridisciplinaire **HAL**, est destinée au dépôt et à la diffusion de documents scientifiques de niveau recherche, publiés ou non, émanant des établissements d'enseignement et de recherche français ou étrangers, des laboratoires publics ou privés.

Experimental Study of the Cr–Hf–Nb System: Liquidus Projection and 1200 °C Isothermal Section

João Carlos Jânio Gigolotti[a,b*], Antonio Augusto Araújo Pinto da Silva[c], Gilberto Carvalho Coelho[d], Carlos Angelo Nunes[d], Jean-Marc Joubert[a]

[a]*Université Paris-Est Créteil, CNRS, ICMPE (UMR 7182), 2 rue Henri Dunant, 94320 Thiais, France.*

[b]*Departamento de Matemática, Física e Computação (DMFC) – Faculdade de Tecnologia (FAT), Universidade Estadual do Rio de Janeiro (UERJ), Rv. Presidente Dutra, km 298, 27537-000, Resende, RJ, Brazil.*

[c]*Instituto de Engenharia Mecânica (IEM), Universidade Federal de Itajubá (UNIFEI), Avenida BPS, 1303, 37500-903, Itajubá, MG, Brasil.*

[d]*Departamento de Engenharia de Materiais (DEMAR), Escola de Engenharia de Lorena (EEL), Universidade de São Paulo (USP), Polo Urbo-Industrial,Gleba AI-6, 12602-810, Lorena, SP, Brazil.*

Abstract

Phase equilibria data from ternary Cr–Nb–X (X = Hf, Ta, Ti, Zr) systems are relevant to the development of Niobium-silicide based composites for use in jet engines. Such systems present at several temperatures a pseudo-binary of Cr_2Nb-Cr_2X Laves phases. This work presents the experimentally determined liquidus projection and the 1200 °C isothermal section for the Cr-Hf-Nb system based on microstructural characterization of as-cast and heat-treated alloys. The microstructural characterization using X-ray diffractometry, scanning electron microscopy and electron probe microanalysis showed four eutectic-type monovariant reactions and two class II invariant reactions in the liquidus projection. The

* Corresponding author. Tel.: +55 24 981081132; E-mail address: carlosjanio@uol.com.br (J.C.J. Gigolotti).

1200 °C isothermal section showed complete solubility between Nb and Hf in (*C*15) phase and one three phase equilibria field.

Key words: Intermetallics; Cr–Hf–Nb system; phase diagram; phase stability; microstructure.

1. Introduction

The search for new materials that improve the performance of high temperature working equipments, such as advanced aeronautical engines, has led to a growing interest in multicomponent based alloys[1,2,3,4]. Niobium-silicide based composites have been considered for use in such applications[5-9], because they show good creep resistance and room temperature fracture toughness, however, the low oxidation resistance has yet to be addressed[6,10]. In these materials, Cr, Hf, Ti, B and Al may be added to improve their properties[1,5,9,11-17]. The Cr_2X Laves compounds (X - Hf, Nb, Ta, Ti, Zr) present, in general, interesting properties such as low density, high corrosion and oxidation resistance as well as microstructural stability for applications at high temperatures[18].

The intermetallic phase observed in Fujita's partial isothermal section for the Cr–Hf–Nb system at 1300 °C[18] (Figure 1) is the Cr_2(Hf,Nb)-rt (rt - room-temperature) Laves phase with *C*15 crystal structure.

In the corresponding constituent binary systems, the accepted proposal for the Cr–Hf phase diagram[19] (Figure 2) is from the assessment by Pavlu et al.[20], in agreement with the experimental data of Svechnikov et al.[21] and Carlson and Alexander[22]. This proposal indicates the stability of (Cr) solid solution, high-temperature Cr_2Hf-ht (*C*14), low-temperature Cr_2Hf-rt (*C*15), (Hf)-ht (bcc) and (Hf)-rt (hcp) phases.

The Cr–Nb system and, particularly, the Cr_2Nb compound[23-37], due to its importance in development of high temperature steels[27] and heat exchangers for coal conversion and gas turbine engine materials[37], has been extensively studied, resulting in several versions of the binary phase diagram. After the early report by Pan[35,36] of the Cr_2Nb (*C*14) existence, many studies have considered a possible Cr_2Nb phase polymorphism involving *C*14 and *C*15 in the phase diagram, for example Ref.[30-34]. However, according to Aufrecht et al.[29], small amounts of contaminations induce the formation of an η-carbide-type phase which led to

earlier erroneous conclusion about the *C*14 ↔ *C*15 phase transformation around 1600 °C. More recently, the Cr–Nb phase diagram has been revised, presenting only the intermediate phase Cr_2Nb (*C*15)[23-28], as shown in Figure 3[23], indicating the stability of (Cr), Cr_2Nb (*C*15) and (Nb) solid phases.

The current proposal for the Hf–Nb phase diagram[38,39], as shown in Figure 4, indicates the stability of (Hf,Nb)-ht and (Hf,Nb)-rt solid phases.

Considering that an adequate balance of properties in engineering materials is strongly dependent on the microstructure, including the phase relationships, the study of sub-systems associated to the Al–B–Cr–Hf–Nb–Si–Ti system is essential for the development of Niobium-silicide based high-temperature materials. It includes the Cr–Hf–Nb system, for which there are two experimental studies in the literature, one by Liu et al.[40] for the 1200 °C isothermal section and the already mentioned Fujita's 1300 °C isothermal section[18].

According to Shangina et al.[41], which reviewed the Cr–Hf–Nb system, "although the temperature of the investigations[18] vary by 100 °C only, the obtained results are mostly different". The proposal by Liu et al.[40] was determined by means of diffusion triple constructed from blocks of pure metals (Hf + Nb, following by addition of Cr) and annealed at 1200 °C for 192 h, while Fujita's proposal[18] was determined using several alloys arc melted and annealed at 1300 °C for 48 h. Liu et al.[40] describe the existence of the two-phase region $NbCr_2$-$HfCr_2$ at 1200 °C with a solubility of ~8.71 at.% Nb in $HfCr_2$ and ~2.54 at.% Hf in $NbCr_2$, whereas Fujita[18] proposes a continues solid solution between $NbCr_2$ and $HfCr_2$ at 1300 °C.

Still according to Shangina et al.[41], regarding the Fujita study[18], "such a comprehensive investigation makes results obtained by Fujita more reliable", therefore, this allowed the authors[41] to build an hypotetical isothermal section of the system at 1300 ° C, on the basis of

Fujita's proposal and the accepted binary systems, in which the presence of a three-phase equilibrium region "(αHf)+β+C15?" is shown.

In addition, the knowledge of specific systems, such as Cr–X (X - Ta, Ti, Zr)[42-45], Hf–X (X - Ta, Ti)[46,47], Zr–X (X - Nb, Ti)[48,49], Cr–Nb/Hf–X (X - Al, Ta, Ti, Zr)[50-59] (Figures 5 and 6) can contribute to understanding the Cr–Hf–Nb system, due to important similarities, such as the presence of intermetallic Laves phases.

2. Experimental Procedures

Nine alloys were prepared by arc-melting small pieces of high purity Cr, Hf and Nb (min. 99.8 wt.%) under high purity argon (min. 99.995%) in a water-cooled copper crucible with non-consumable tungsten electrode and titanium getter to remove residual O_2/H_2O/N_2. Each alloy was melted at least five times in an effort to produce homogeneous ingots of 3-4 g.

After the melting process, each alloy was weighed to verify possible mass loss, which was found to be negligible (< 1.0 wt.%).

One part of each as-cast (AC) alloy was kept for the liquidus projection investigation and another part for heat treatment, as follows: (a) the samples were separately encapsulated into quartz tubes with a titanium getter, filled with argon after vacuum; (b) the finished capsule was subjected to a second encapsulation using the same previous procedures. The tubes were accommodated in the uniform temperature zone of an alumina tubular furnace for heat treatment of the alloys at 1200 °C for 720 h.

The AC and heat-treated (HT) alloys were characterized by scanning electron microscopy (SEM) and X-ray diffraction (XRD). HT alloys were also characterized by electron beam microprobe analysis (EPMA).

For the XRD analysis the samples were mechanically ground and sieved to below 80 mesh. The experiments were performed in a D8 Advance Bruker diffractometer, at room

temperature, with CuKα radiation and graphite monochromator. The measurement conditions were: $5^{o} < 2\theta < 120^{o}$, 0.04° ($2\theta$ step) and 2s integration time. The phases in each sample were identified based on simulated diffraction patterns obtained from the PowderCell for Windows (version 2.4)[60] software using the crystallographic data shown in Table 1[61-77]. The XRD results were refined by the Rietveld method[78] with FullProf Suite[79] software.

For the analysis via SEM and EPMA, the alloys were prepared following standard metallographic procedures, i.e., hot mounting, grinding in the #320-#1200 sequence with SiC paper, polishing with colloidal silica suspension (OP-S). The alloys were characterized via SEM in back-scattered electron mode (BSE) with accelerating voltage of either 15 kV or 25 kV; beam current of 20 nA. The phases in each alloy were identified in the SEM/BSE micrographas based on the different image contrasts of the different phases, associated to different average atomic number. The alloys were characterized via EPMA in a CAMECA SX 100 instrument.

Comparison of AC and HT alloys microstructures allowed to evaluate the microstructural changes during heat treatment and to estimate if the HT alloys reached thermodynamic equilibrium.

The fields in the isothermal section at 1200 °C of the Cr–Hf–Nb system were determined taking into account: (a) the EPMA measurements from phases present in HT alloys; (b) the amount of each particular phase in HT alloys, which was determined in two ways: (1) using the lever rule, from the alloy composition and the positions of tie-triangle vertices or tie-line extremity that define the phase equilibria field; (2) through the refinement of the XRD data by the Rietveld method[78] with FullProf Suite program[79]. The values obtained in (1) and (2) showed similar results.

3. Results and discussion

Table 2 shows the phases observed in the AC alloys and the invariant reactions associated to their solidification paths. Table 3 shows the phases observed in HT alloys and the results of EPMA. Figure 7 exhibit the Cr–Hf–Nb liquidus projection and Figure 8 the isothermal section at 1200 °C, both proposed from results obtained in the present work.

3.1 Cr–Hf–Nb liquidus projection

The results of the alloys 01AC-04AC allowed to determine the eutectic-type monovariant reactions L ⇄ (Cr) + *C*14 (**e1**-**II1** line in Figure 7) and L ⇄ (Cr) + *C*15 (**II1**-**e4**), the class II invariant reaction L + *C*14 ⇄ (Cr) + *C*15 (**II1**) as well the *C*14, *C*15 and (Cr) solid solution primary precipitation fields, in the Cr-rich region. The micrographs of alloys 01AC-03AC (Figures 9a-9c), together with the XRD results (Figures 10a-10c), allow to identify the primary precipitation of *C*14 phase. The presence of C15 phase in these alloys indicates that the final solidification should occur through the (Cr) + 15 eutectic type-precipitation associated to the (**II1-e4**) monovariant line. At least in the case of alloys 01AC and 02AC, a second solidification event involving (Cr) + C14 (**e1**-**II1**) eutectic-like precipitation should have taken place. While alloys 01AC and 03AC show a large amount of primary *C*14 precipitates, comparatively, alloy 02AC (Figure 9b) presents much lower quantity of primary *C*14, which indicates that its composition is close to the **e1**-**II1** monovariant line.

The increasing amount of *C*15 phase in alloys 01AC-04AC for higher Nb contents (Table 2), difficult to distinguish in the corresponding diffractograms, Figures 10a-10c (alloys 01AC-03AC), is best characterized in Figure 10d (alloy 04AC). The micrograph of the 04AC alloy (Figure 9d) with the XRD results (Figure 10d), shows the primary precipitation of *C*14 followed by a peritectic-type precipitaion of *C*15 and an eutectic-type structure, possibly *C*15

+ (Cr) (**II1**-**e4**), in the last solidified region. It suggests a peritectic-type nature for the **m**-**II1** line in Figure 7.

The results of alloys 05AC-08AC (Figures 11 and 12) and 09AC allowed to determine the eutectic-type monovariant reactions L ⇄ (Hf,Nb)-ht + *C*15 (**e3**-**II2**) and L ⇄ (Hf,Nb)-ht + *C*14 (**II2**-**e2**), the class II invariant reaction L + *C*15 ⇄ (Hf,Nb)-ht + *C*14 (**II2**) as well as the *C*14, *C*15 and (Hf,Nb)-ht primary precipitation fields. In addition, it also identified the peritectic-type nature of the **m**-**II2** line.

The micrograph of 05AC alloy (Figure 11a) and XRD results (Figure 12a), clearly suggests the primary precipitation of *C*14 folowed by the peritectic-type precipitation of *C*15 as the liquid composition crosses the **m**-**II2** line, the solidification finishing possibly through *C*15 + (Hf,Nb)-ht (**e3**-**II2**) eutectic-type precipitation.

The *C*15 phase is present in a larger amount in alloy 06AC than in alloy 05AC (seen from a comparison of the diffractograms in Figure 12b and 12a) since its composition is very close to the **m**-**II2** line and thus, it presents a long solidification path through the L+ *C*15 two-phase field. The microstructure of this alloy (Figure 11b), allows to infer the primary precipitation of *C*14, followed by the peritectic-type precipitation of *C*15, then *C*15 + (Hf,Nb)-ht (**e3**-**II2**), and a finer one, possibly *C*14 + (Hf,Nb)-ht, in the last solidified region, suggesting the sequence of eutectic-type reactions L ⇄ (Hf,Nb)-ht + *C*15 (**e3**-**II2**) and L ⇄ (Hf,Nb)-ht + *C*14 (**II2**-**e2**).

The diffractogram of alloy 07AC (Figure 12c), shows *C*14, (Hf,Nb)-ht and (Hf,Nb)-rt phases. The corresponding microstructure (Figure 11c) has a characteristic fine eutectic-type morphology from L ⇄ (Hf,Nb)-ht + *C*14 reaction, associated to **II2**-**e2** monovariant line. The predominance of this eutectic structure indicates that 07AC alloy composition is very close to the **II2**-**e2** monovariant eutectic-type line, and the absence of the *C*15 phase proves that this monovariant line follows the **II2** → **e2** direction.

The diffractogram of alloy 08AC (Figure 12d) shows the (Hf,Nb)-ht and (Hf,Nb)-rt phases. The corresponding microstructure (Figure 11d), shows the primary precipitation of (Hf,Nb)-ht phase and, in sequence, its partial allotropic transformation to (Hf,Nb)-rt phase. Alloy 09AC showed complete solidification of the liquid to the (Hf,Nb)-ht phase and together with alloy 08AC defined the primary precipitation field of (Hf,Nb)-ht.

The proposal of this work for the Cr–Hf–Nb liquidus projection (Figure 7) with respect to monovariant eutectic reactions L ⇄ (Cr) + *C*14 / *C*15 (**e1**-**Il1** and **Il1**-**e4**) and L ⇄ (Hf,Nb)-ht + *C*15 / *C*14 (**e3**-**Il2** and **Il2**-**e2**), class II invariant reactions L + *C*14 ⇄ (Cr) + *C*15 (**Il1**) and L + *C*15 ⇄ (Hf,Nb)-ht + *C*14 (**Il1**) and the primary precipitation fields of (Cr), (Hf,Nb)-ht, *C*14 and *C*15 allows a comparison with the proposals developed for the liquidus projections of the Cr–Nb–Al[58], Cr–Hf–Ti[59] and Cr–Nb–Zr (hypothetical) systems (Figures 6a-6c), because their important similarities.

Starting from the constituent binary systems, the Cr–X (X - Hf, Nb, Zr, Ti)[19,20,23,42-44], they present (Cr), (X)-bcc and the intermetallics Laves *C*14[19,20,42,44], *C*15[23,42-44] and *C*36[42,43]. The liquidus ↔ solidus reactions are *L* ↔ (bcc)[19,20,23,42-45], the congruent *L* ↔ *C*14[19,20,42,44] and *L* ↔ *C*15[23], the eutectic *L* ↔ *C*14 + (bcc)[19,20,44], *L* ↔ *C*15 + (bcc)[23,42] and *L* ↔ *C*36 + (bcc)[42]. The Cr–Ti[43], specifically, presents the *solidus* ↔ *solidus* (Cr,Ti)-ht (bcc) ↔ *C*14 and the eutectoid (Cr,Ti)-ht ↔ *C*15 + (Ti)-rt hcp. Similarly, in Hf–X (X – Nb, Ti, Ta)[38,46,47] and Zr–X (X - Nb, Ti)[48,49] systems, only the *L* ↔ (bcc - complete solid solubility) reaction characterizes the diagrams in high temperature range (approximately > 1200 °C).

The proposed liquidus projection of the Cr–Nb–Al system[58] (Figure 6a), Cr–Hf–Ti[59] (Figure 6b) and Cr–Nb–Zr (hypothetical) (Figure 6c), built from the Cr–Nb–Zr *solidus* projection[50] (Figure 6d) and the corresponding binaries[23,42,49], shows in the intermediate region the primary precipitation fields of *C*15, *C*14, with varied extension, and *C*36, just in

Cr–Nb–Zr, limited by the corresponding monovariant L ↔ (bcc) + Laves, and the invariant class II reactions L + *C*14/*C*15 ↔ (bcc) + *C*15/*C*14 and L + *C*15 ↔ (bcc) + *C*36, in Cr–Nb–Zr.

3.2 Cr–Hf–Nb isothermal section at 1200 °C

The results obtained for the HT alloys show that, in general, they have reached the thermodynamic equilibrium or came close to it. This is verified by the phase transformations and important mass transport occurred during heat-treatment of the AC alloys, supported by data in Table 2 and 3 and the micrographs shown in this section.

The results of the alloys 01HT-04HT allowed to determine the two-phase equilibrium field (Cr)–(*C*15) and the solubility limits of (Cr) and (*C*15), in the Cr-rich region (Figure 8). The SEM images of these alloys (Figures 13a-13d) show heterogeneous microstructures that can define the two-phase equilibrium field (Cr)–(*C*15) according to XRD results (Figures 14a-14d), that show the phases (Cr), *C*15 and a very small quantity of remaining *C*14 from the as-cast alloys. Comparing these heat-treated alloys with the corresponding as-cast alloys, there is a clear transformation of *C*14 phase into *C*15, shown by the decrease/disappearance of *C*14 peaks intensity and the presence of well-defined *C*15 peaks in the HT alloys.

The results of alloys 05HT and 06HT allowed to determine the two-phase equilibrium field (Hf,Nb)-ht–(*C*15) and the solubility limits of the (Hf,Nb)-ht and (*C*15). The micrographs of 05HT and 06HT alloys (Figure 15a and 15b), show heterogeneous microstructures mostly involving the (Hf,Nb)-ht and (*C*15) phases, with the almost total disappearance of the *C*14 phase for the benefit of *C*15 phase. The XRD results of these alloys (Figure 16a and 16b), confirm these observations. The diffractograms show the (Hf,Nb)-ht and (*C*15) phases in both alloys and small intensity *C*14 peaks only in the 05HT alloy. These

observations demonstrate that 05HT and 06HT alloys tend to the thermodynamic equilibrium between (Hf,Nb)-ht and (*C*15) phases.

The results of alloy 07HT allowed to determine the two-phase equilibrium field (Hf,Nb)-rt–*C*15 and the solubility limits of (Hf,Nb)-rt and (*C*15) phases. The SEM image of this alloy (Figure 15c), shows a heterogeneous microstructure involving (Hf,Nb)-rt and *C*15 phases, with a very clear microstructure transformation from the as-cast alloy in Figure 11c. The corresponding XRD data (Figure 16c), presents (Hf,Nb)-rt and (*C*15) phases, which, compared with the XRD data of 07AC alloy (Figure 12c), indicates the complete transformation of *C*14 and (Hf,Nb)-ht phases into *C*15 and (Hf,Nb)-rt phases.

The results of alloy 08HT allowed to determine the (Hf,Nb)-rt–(*C*15)–(Hf,Nb)-ht three-phase equilibrium field and the solubility limits of (Hf,Nb)-rt and (Hf,Nb)-ht, in the Hf-Nb-rich region, and (*C*15) in the intermediate region. SEM image of this alloy (Figure 15d), based on the corresponding XRD data, Figure 16d, shows an heterogeneous microstructure of (Hf,Nb)-rt, (*C*15) and (Hf,Nb)-ht phases. The small amount of (*C*15) (5.0 vol.%) present in the alloy demonstrates that it is located very close to the (Hf,Nb)-rt–(Hf,Nb)-ht tie-triangle edge, which allows to determine the corresponding (Hf,Nb)-rt–(*C*15)–(Hf,Nb)-ht three-phase equilibrium field.

When comparing 08AC with 08HT samples, it is remarkable that (Hf,Nb)-rt and (Hf,Nb)-ht phases have both clearly suffered coarsening (Figure 15d). These results prove the thermodynamic equilibrium between (Hf,Nb)-rt, (Hf,Nb)-ht and *C*15 phases in the 08HT alloy.

The results of alloy 09HT (Table 3) allowed to determine the (Hf,Nb)-ht single phase field in the Hf-Nb-rich region. The XRD data of this alloy just presented the (Hf,Nb)-ht phase and the corresponding SEM images showed a homogeneous microstructure involving only this phase.

Concerning the Cr–Hf–Nb isothermal section at 1200 °C, the results show good agreement with the existing partial isothermal section at 1300 °C for this system[18] (Figure 1) and are consistents in relation to isothermal sections of other similar systems, Cr–Nb–Zr (1300 °C)[52], Cr–Nb–Ti (1300 °C)[55], Cr–Nb–Ta (1500 °C) and Cr–Hf–Ti (1200 °C)[59] (Figures 5a-5d).

With regard to the single phase fields (Cr), (Hf,Nb)-ht, (*C*15) and the two-phase equilibria (Cr)–(*C*15) and (*C*15)–(Hf,Nb)-ht, the similarities are clear with the proposals for Cr–Nb–X (X - Zr, Ti, Ta)[52,55,57], which show the (Cr) and (Nb,X)-bcc fields and in the intermediate region the pseudobinary *C*15 with several solubility ranges (Figures 5a-5c). In Cr–Nb–Zr isothermal section at 1300 °C[52], Figure 5a, particularly, there is a noticeable increase in the solubility range of (*C*15) in intermediate compositions, advancing over the (*C*15)–(Zr,NB)-bcc field, as well as (*C*15) advances over the (*C*15)–(Hf,Nb)-ht in Cr–Hf–Nb system.

In the specific case of the fields (Hf,Nb)-rt, (Hf,Nb)-rt–(Hf,Nb)-ht, (*C*15)–(Hf,Nb)-rt and (Hf,Nb)-rt–(*C*15)–(Hf,Nb)-ht, a comparison with the Cr–Hf–Ti (1200 °C)[59] system can be made. Starting from the constituent binary systems, the Hf–X (X - Nb, Ti)[38,46] diagrams are characterized by the existence, at 1200 °C, of the fields (Hf,X)-ht (bcc), (Hf,X)-ht (bcc)–(Hf,X)-rt (hcp) and (Hf,X)-rt (hcp), then the formation of two-phase equilibrium field (Hf,X)-ht–(Hf,X)-rt in the Cr–Hf–X ternary systems (X - Nb, Ti) is plausible and would suggest, on the other hand, the formation of three-phase equilibrium field (Hf,X)-ht–(*C*15)–(Hf,X)-rt. However, the discrepancy between the diagrams Hf–Nb and Cr–Hf–Nb in the solubility of Hf in Nb (Hf,Nb)-ht, at 1200 °C, is notorious, which cast doubt on the reported binary solubility of Hf in Nb that should be reevaluated.

The large mass transport that occurred among the phases present in the AC alloys and corresponding HT alloys, Tables 2 and 3, respectively, confirms the effectiveness of the method used to produce equilibrated alloys at 1200 °C, which gives credence to the results.

The use of selected and arc-melted alloys, allows accurate evaluation of phase relations, especially for the determination of the phase equilibria in an isothermal section not much higher than 50% of the average melting temperatures of the components and congruently melting compounds, (*C*15). This assertion is demonstrated by the results observed in all of the alloys in which significant mass transport and almost complete phase transformation was observed with the applied heat treatment. However, it is suggested to reassess the system using the diffusion method, taking into account that the combination of methods seems adequate to obtain more accurate result[80].

4. Conclusion

This work has carried out a detailed investigation on the microstructure of as-cast and heat-treated Cr-Hf-Nb alloys to evaluate the liquidus projection and the isothermal section at 1200 °C of the Cr–Hf–Nb system. The results defined the (Cr), *C*14, *C*15 and (Hf,Nb)-ht primary precipitation fields in the liquidus projection and the ternary invariant reactions L + *C*14 ↔ (Cr) + *C*15 and L + *C*15 ↔ (Hf,Nb)-ht + *C*14. The following equilibrium fields were identified on the isothermal section at 1200 °C of (Cr), (Hf,Nb)-ht, (Hf,Nb)-rt, (*C*15), (Cr) + (*C*15), (Hf,Nb)-ht + (*C*15), (Hf,Nb)-rt + (*C*15), (Hf,Nb)-ht + (Hf,Nb)-rt and (Hf,Nb)-ht + (*C*15) + (Hf,Nb)-rt.

Acknowledgements

The authors thank CNPq (Conselho Nacional de Desenvolvimento Cientíco e Tecnológico – Brazil) for the financial support through scholarship # 249666/2013-8 of "Ciência Sem Fronteiras" Program.

References

[1] C.M. Ward-Close, R. Minor, and P.J. Doorbar, Intermetallic-Matrix Composites – A Review, *Intermetallics*, 1996, 4(3), p 217-229.

[2] M.R. Jackson, B.P. Bewlay, R.G. Rowe, D.W. Skelly, and H.A. Lipsitt, High-Temperature Refractory Metal–Intermetallic Composites, *J. Met.*, 1996, 48(1), p 39-43.

[3] J-C. Zhao and J.H. Westbrook, Ultrahigh-Temperature Materials for Jet Engines, *MRS Bull.*, 2003, 28(9), p 622-630.

[4] D.M. Dimiduk and J.H. Perepezko, Mo–Si–B Alloys: Developing a Revolutionary Turbine-Engine Material, *MRS Bull.*, 2003, 28(9), p 639-645.

[5] P.R. Subramanian, M.G. Mendiratta and D.M. Dimiduk, The Development of Nb–Based Advanced Intermetallic Alloys for Structural Applications, *J. Met.*, 1996, 48(1), p 33-38.

[6] M.G. Mendiratta, and D.M. Dimiduk, Strength and Toughness of Nb/Nb_5Si_3 Composite, *Metall. Mater. Trans.*, 1993, 24(A), p 501-504.

[7] B.P. Bewlay, M.R. Jackson, J-C. Zhao, and P.R. Subramanian, A Review of Very-High-Temperature Nb–Silicide–Based Composites, *Metall. Mater. Trans.*, 2003, 34(A), p 2043-2052.

[8] B.P. Bewlay, M.R. Jackson, and M.F.X. Gigliotti, Niobium Silicide High Temperature in-situ Composites, *Intermetallic compounds, principles and practice: progress*, 2002, 3, p 541.

[9] B.P. Bewlay, M.R. Jackson, and C.L. Briant, Deformation Mechanisms in Niobium Silicide-Based Composites – Final Report, *AFOSR*, 2001, p 1-23.

[10] M.G. Mendiratta, and D.M. Dimiduk, Microstructures and Mechanical Behavior of Two-Phase Niobium Silicide–Niobium Alloys, *Mater. Res. Soc. Symp. Proc.*, 1989, 133, p 441-446

[11] N. Vellios, and P. Tsakiropoulos, The Role of Sn and Ti Additions in the Microstructure of Nb-18Si Base Alloys, *Intermetallics*, 2007, 15, p 1518-1528.

[12] K. Zelenitsas and P. Tsakiropoulos, Effect of Al, Cr and Ta Additions on the Oxidation Behavior of Nb–Ti–Si In Situ Composites at 800 ºC, *Mat. Sci. Eng. A-Struct.*, 2006, 416 (1-2), p 269-280.

[13] K. Zelenitsas, and P. Tsakiropoulos, Study of the Role of Al and Cr Additions in the Microstructure of Nb–Ti–Si in Situ Composites, *Intermetallics*, 2005, 13(10), p 1079-1095.

[14] B.P. Bewlay, M.R. Jackson, and H.A. Lipsitt, The Balance of Mechanical and Environmental Properties of a Multielement Niobium–Niobium Silicide-Based In Situ Composite, *Metall. Mater. Trans. – A*, 1996, 27(12), p 3801-3808.

[15] L. Su, L. Jia, J. Weng, Z. Hong, C. Zhou, and H. Zhang, Improvement in the Oxidation Resistance of Nb–Ti–Si–Cr–Al–Hf Alloys Containing Alloyed Ge and B, *Corros. Sci.*, 2014, 88, p 460-465.

[16] J.C. Zhao, B.P. Bewlay, M.R. Jackson and L.A. Peluso, Alloying and Phase Stability in Niobium Silicide In-Situ Composites, Structural Intermetallics, 2001, p 483-490.

[17] J.–C. Zhao, M.R. Jackson, and L.A. Peluso, Mapping of the Nb–Ti–Si Phase Diagram Using Diffusion Multiples, *Mat. Sci. Eng. A-Struct.*, 2004, 372(1-2), p 21-27.

[18] M. Fujita, Y. Kaneno, and T. Takasugi, Phase field and room-temperature mechanical properties of C15 Laves phase in Nb–Hf–Cr and Nb–Ta–Cr alloy systems, *J. Alloy. Compd.*, 2006, 424, p 283-288.

[19] H. Okamoto, Supplemental Literature Review of Binary Phase Diagrams: Al–Bi, Al–Dy, Al–Gd, Al–Tb, C–Mn, Co–Ga, Cr–Hf, Cr–Na, Er–H, Er–Zr, H–Zr and Ni–Pb, *J. Phase Equilib. Diff.*, 2014, 35(3), p 348-349.

[20] J. Pavlů, J. Vřešt'ál, and M. Šob, Thermodynamic modeling of Laves phases in the Cr-Hf and Cr–Ti systems: Reassessment using first-principles results, *CALPHAD*, 2010, 34, p 215-221.

[21] V.N. Svechnikov, A.K. Shurin and G.P. Dmitrieva, The Phase Diagram of Hafnium-Chromium, Phase Changes in Metals and Alloys, Akademii Nauk Ukrainy SSR, 1965, p 169-162.

[22] O.N. Carlson, and D.G. Alexander, The Hafnium–Chromium System, *J. Less Common Met.*, 1968, 15, p 361-370.

[23] P. Lafaye, C. Toffolon-Mascleta, J.-C. Crivellob, and J.-M. Joubert, Thermodynamic modelling of the Cr–Nb–Sn system, *CALPHAD*, 2017, 57, p 37-45.

[24] E.A. Syutkin, A. Jacob, C. Schmetterer, A.V. Khvan, B. Hallstedt, and A.T. Dinsdale, Experimental determination of the thermodynamic properties of the Laves phases in the Cr–Fe–Nb system, *Thermochim. Acta*, 2016, 624, p 47-54.

[25] Y. Peng, P. Zhou, M. Bu, W. Zhang, and Y. Du, A thermodynamic evaluation of the C–Cr–Nb system, *CALPHAD*, 2016, 53, p 10-19.

[26] H.-J. Lu, W.-B. Wang, N. Zou, J.-Y. Shen, X.-G. Lu, and Y.-L. He, Thermodynamic modeling of Cr–Nb and Zr–Cr with extension to the ternary Zr–Nb–Cr system, *CALPHAD*, 2015, 50, p 134-143.

[27] C. Schmetterer, A. Khvan, A. Jacob, B. Hallstedt, and T. Markus, A New Theoretical Study of the Cr–Nb system, *J. Phase Equilib. Diff.*, 2014, 35, p 434-444.

[28] F. Stein, C. He, and I. Wossack, The liquidus surface of the Cr–Al–Nb system and re-investigation of the Cr–Nb and Al–Cr phase diagrams, *J. Alloy. Compd.*, 2014, 598, p 253-265.

[29] J. Aufrecht, A. Leineweber, A. Senyshyn, and E.J. Mittemeijer, The Absence of a Stable Hexagonal Laves Phase Modification ($NbCr_2$) in the Nb–Cr System, *Scr. Mater.*, 2010, 62(5), p 227-230.

[30] K. Li, S. Li, Y. Xue, and H. Fu, Microstructure characterization and mechanical properties of a Laves-phase alloy based on Cr_2Nb, *Int. J. Refract. Hard Met.*, 2013, 36, p 154-161.

[31] N. David, Y. Cartigny, T. Belmonte, J.M. Fiorani, and M. Vilasi, Thermodynamic description of the Cr–Nb–Si isothermal section at 1473 K, *Intermetallics*, 2006, 14, p 464-473.

[32] J.G. Costa Neto, S.G. Fries, H.L. Lukas, S. Gama, and G. Effenberg, Thermodynamic optimisation of the Nb–Cr system, *CALPHAD*, 1993, 17, p 219-228.

[33] D.J. Thoma, and J.H. Perepezko, An experimental evaluation of the phase relationships and solubilities in the Nb–Cr system, *Mat. Sci. Eng. A-Struct.*, 1992, 156, p 97-108.

[34] M. Venkatraman and J.P. Neumann, Cr–Nb (Chromium–Niobium), *Binary Alloy Phase Diagrams*, 2nd Ed., Ed. T.B. Massalski, 1990, 2, p 1298-1299.

[35] V.M. Pan, Polymorphic Transformation in $NbCr_2$, *Fizika Metallov i Metallovedenie*, 1961, 12 (3), p 455-457, in Russian.

[36] V.M. Pan, Definition of Equilibrium Diagrams for Cr–Nb and $NbCr_2$–Ni_3Nb Systems, *Dopovidi Akademii Nauk Ukrains'koi RSR*, 1961, 4, p 332-334, in Russian.

[37] D.J. Thoma, C.C. Katherine, P.G. Kotula, T.E. Mitchell, J.M. Wills, A. Ormeci, S.P. Chen and R.C. Albers, Theoretical and experimental investigation on the low-temperature properties of NbCr*2* Laves phase, Los Alamos FY1996 LDRD Progress Report, p 12-13, https://inis.iaea.org/collection/NCLCollectionstore/_Public/29/006/29006513.pdf.

[38] H. Okamoto, Hf–Nb Phase Diagram, *J. Phase Equilib.*, 1998, 19, p 288.

[39] A. Fernandez Guillermet, Gibbs energy coupling of phase stability and thermochemistry in the Hf–Nb system, *J. Alloy. Compd.*, 1996, 234, p 111-118

[40] L. Liu, R. Wang, D. Wen, Y. Feng, Determination of Isothermal Sections of Nb–Cr–Hf Ternary System at 1473 K, *J. Central South Univ. Technol.*, Sci. Technol. (China), 2006, 37(4), p 646-649, in Chinese.

[41] D. Shangina, N. Bochvar, O. Dovbenko, Cr–Hf–Nb Ternary Phase Diagram Evaluation, in MSI Eureka, G. Effenberg (Ed.), Materials Science International, Stuttgart, 2017, ID: 10.52516.1.5.

[42] H. Okamoto, Supplemental Literature Review of Binary Phase Diagrams: B–Fe, Cr–Zr, Fe–Np, Fe–W, Fe–Zn, Ge–Ni, La–Sn, La–Ti, La–Zr, Li–Sn, Mn–S and Nb–Re, *J. Phase Equilib. Diff.*, 2016, 37(5), p 621-634.

[43] H. Okamoto, Supplemental Literature Review of Binary Phase Diagrams: Ag–Li, Ag–Sn, Be–Pu, C–Mn, C–Si, Ca–Li, Cd–Pu, Cr–Ti, Cr–V, Cu–Li, La–Sc and Li–Sc, *J. Phase Equilib. Diff.*, 2017, 38(1), p 70-81.

[44] J. Pavlů, J. Vřešt'ál, and M. Šob, Re-modeling of Laves phases in the Cr–Nb and Cr–Ta systems using first-principles results, *CALPHAD*, 2009, 33(1), p 179-186.

[45] C. Sha, M. Bu, H. Xu, Y. Du, S. Wang, and G. Wen, A thermodynamic modeling of the C–Cr–Ta ternary system, *J. Alloy. Compd.*, 2011, 509(20), p 5996-6003.

[46] H. Okamoto, Hf–Ti (Hafnium–Titanium), *J. Phase Equilib.*, 1997, 18(6), p 672.

[47] A.F. Guillermet, Gibbs energy modelling of the phase diagram and thermochemical properties in the Hf–Ta system, *Z. Metallkd.*, 1995, 86(6), p 382-387.

[48] A.F. Guillermet, Thermodynamic analysis of stable phases in the Zr–Nb system and calculation of the phase diagram, *Z. Metallkd.*, 1991, 82, p 478-487.

[49] H. Okamoto, Supplemental Literature Review of Binary Phase Diagrams: Al–Ni, B–Hf, Ca–Sc, Cr–Sc, Fe–Rh, Hf–Mn, La–Sb, Ni–Re, Ni–Sm, Ni–Zr, Sb–Tb and Ti–Zr, *J. Phase Equilib. Diff.*, 2019, p 1-12.

[50] M.M. Savel'yeva, and N.V. Grum-Grzmaylo, Phase diagram of Nb–Zr–Cr alloys, *Metally*, translated from Izvestiya Akademii Nauk SSSR, 1969, 1, p 117-120.

[51] W.-Y. Kim, and T. Takasugi, Laves phase fields in Cr–Zr–Nb and Cr–Zr–Hf alloy systems, *Scr. Mater.*, 2003, 48, p 559-563.

[52] W.-B. Wang, H.-J. Lu, J.-Y. Shen, X.-G. Lu, and Y-L. He, Experimental investigation of phase equilibria in the Zr–Nb–Cr system at 1573 K and 1373 K, *J. Nucl. Mater.*, 2015, 465, p 626-632.

[53] H.-J. Lu, W.-B. Wang, N. Zou, J.-Y. Shen, X.-G. Lu, and Y-L. He, Thermodynamic modeling of Cr–Nb and Zr–Cr with extension to the ternary Zr–Nb–Cr system, *CALPHAD*, 2015, 50, p 134-143.

[54] K.I. Shakhova and P.B. Budberg, Investigation of alloys of the ternary Ti–Nb–Cr system, titanium and its alloys, English translation of *Titan I EGO Splavy*, Moscow, 1966, 10, p 34-39.

[55] L. Kaufman, and H. Nesor, Calculation of superalloy phase diagrams: Part III, *Metall. tran.*, 1975, 6(A), p 2115-2122.

[56] P. Kotula, C.B. Carter, K. Chen, D.J. Thoma, F. Chu, and T.E. Mittchell, Defects and Site Occupancies in Nb–Cr–Ti C15 Laves Phase Alloys, *Scr. Mater.*, 1998, 39(4-5), p 619-623.

[57] W. Rostoker, Phase Equilibria in refractory metal systems, *Metallurgical Society Conferences*, Proceedings, 1961, 11, p 3-23.

[58] F. Stein, C. He, and I. Wossack, The Liquidus Surface of the Cr–Al–Nb System and Re-investigation of the Cr–Nb and Al–Cr Phase Diagrams, *J. Alloy. Compd.*, 2014, 598, p 253-265.

[59] C.P. Wang, X.P. Li, S.Y. Yang, J. Li, Y. Lu, Z. Shi, Y.W. Kang, and X.J. Liu, Experimental Investigation and Thermodynamic Calculation of the Phase Equilibria in the Cr–Hf–Ti Ternary System, *J. Phase Equilib. Diff.*, 2013, 34, p 375-384.

[60] W. Kraus and G. Nolze, PowderCell for Windows (version 2.4), *Federal Institute for Materials research and testing*, Berlin, 1999.

[61] P. Villars and L.D. Calvert, Pearson's handbook of crystallographic data for intermetallic phases, 2nd ed. Materials Park (OH): *ASM International*, 1991.

[62] A. Pialoux, M.L. Joyeux, and G. Cizeron, Etude du Comportement du Niobium Sous Vide par Difraction des Rayons X a Haute Temperaturevsky, *J. Less Common Met.*, 1982, 87, p 1-9.

[63] H. Rassaerts, F. Benesovsky and H. Novotny, Untersuchungen in den Systemen Niob- und Tantal-Chrom-Kohlenstoff, *Planseeberichte für Pulvermetallurgie*, 1965, 13, p 199-206, in German.

[64] M.E. Straumanis, and C.C. Weng, The Precise Lattice Constant and the Expansion Coefficient of Chromium between +10 and +60 °C, *Acta Crystallogr.*, 1955, p 367-371.

[65] T.B. Massalski, H. Okamoto, P.R. Subramanian, and L. Kacprzak, Eds., *Binary Alloy Phase Diagrams*, 2nd ed., Materials Park (OH): ASM International, 1990.

[66] R.G. Ross, and W. Hume Rothery, High Temperature X-Ray Metallography, *J. Less Common Met.*, 1963, 5, p 258-270.

[67] H.F. McMurdie, M.C. Morris, E.H. Evans, B. Paretzkin, W. Wong Ng, Y. Zhang and C.R. Hubbard, Standard X-Ray Diffraction Powder Patterns from The JCPDS Research Associateship, *Powder Diffraction*, 1987, 2, p 41-52.

[68] R.P. Elliot, Laves-Type Phases of Hafnium, *Trans. Am. Soc. Met.*, 1961, 53, p 321-329.

[69] E. Rudy, and S. Windisch, The Phase Diagrams Hafnium–Vanadium and Hafnium–Chromium, *J. Less Common Met.*, 1968, 15, p 13-27.

[70] P.A. Suprunenko, V.Ya. Markiv, and T.M. Tavetkova, Magnetic and X-Ray Diffraction Study of Laves Phases in the Ternary Systems (Ti, Zr, Hf)–Cr–Al, *Metally*, Translated from Izvestiya Akademii Nauk SSSR, 1984, 1, p 207-210.

[71] H. Rassaerts, F. Benesovsky and H. Novotny, Untersuchungen in den Systemen Titan- und Hafnium-Chrom-Kohlenstoff, *Planseeberichte für Pulvermetallurgie*, 1966, 14, p 23-28, in German.

[72] R.P. Elliott, and W. Rostoker, The Occurrence of Laves-Type Phases Among Transition Elements, *Tran. Am. Met.*, 1958, 50, p 617-633.

[73] S.A. Minayeva, and P.B. Budberg, Phase Equilibrianin the V–Hf–Cr System, *Metally*, Translated from Izvestiya Akademii Nauk SSSR, 1975, 3, p 179-182.

[74] Z. Blazina, and R. Trojko, Structural Investigation of the $Nb_{1-x}Si_xT_2$ and $Nb_{1-x}Al_xT_2$ (T = Cr, Mn, Fe, Co, Ni) Systems, *J. Less Common Met.*, 1986, 119, p 297-305.

[75] P.B. Budberg, and S.P. Alisova, Investigation of the $TaCr_2$–$ZrCr_2$ and $TaCr_2$–$NbCr_2$ Systems, *Metally*, Translated from Izvestiya Akademii Nauk SSSR, 1969, 3, p 140-142.

[76] L.I. Kornilov, S.P. Alisova, and P.B. Budberg, Equilibrium Phase Diagram for the $ZrCr_2$ and $NbCr_2$–$ZrCr_2$ Metallic Compound System, *Inorg. Mater.*, Translated from Izvestiya Akademii Nauk SSSR, Neorganicheskie Materially, 1965, 1(12), p 1993-1995.

[77] A.E. Dwight, Alloying Behavior of Columbium, *Metallurgical Society Conferences*, Proceedings, 1961, 10, p 383-405.

[78] H.M. Rietveld, A profile refinement method for nuclear and magnetic structures, *J. Appl. Crystallogr.*, 1969, 2(b), p 65-71.

[79] J. Rodriguez-Carvajal, Recent Advances in Structure Determination by Neutron Powder Diffraction + FullProf, Physica B: Condensed Matter, 1993, 192 (1-2), p 55-56, in: http://www.ill.eu/sites/fullprof/, accessed January 29, 2020.

[80] A.A. Kodentsov, G.F. Bastin, and F.J.J. van Loo, The diffusion couple technique in phase diagram determination, *J. Alloy. Compd.*, 2001, 320(2), p 207-217.

Figure Captions

Figure 01 – Experimental isothermal section of the Cr–Hf–Nb system at 1300 °C redrawn/adapted from Fujita et al.[18].

Figure 02 – Assessed Cr–Hf phase diagram redrawn/adapted from Pavlu et al.[19,20].

Figure 03 – Assessed Cr–Nb phase diagram redrawn/adapted from Lafaye et al.[23].

Figure 04 – Experimental Hf–Nb phase diagram redrawn/adapted from Okamoto[38].

Figure 05 – Some Cr–Nb–X (X → metal) and Cr–Hf–Ti ternary diagrams redrawn/adapted: (a) Cr–Nb–Zr isothermal section at 1300 °C from Wang et al.[52]; (b) Cr–Nb–Ti isothermal section at 1300 °C from Kaufman et al.[55]; (c) Cr–Nb–Ta isothermal section at 1500 °C from Rostoker[57]; (d) Cr–Hf–Ti isothermal section at 1200 °C from Wang et al.[59].

Figure 06 – Some Cr–Nb–X (X → metal) and Cr–Hf–Ti ternary diagrams redrawn/adapted: (a) Cr–Nb–Al liquidus projection from Stein et al.[58]; (b) Cr–Hf–Ti liquidus projection from Wang et al.[59]; (c) hypothetical Cr–Nb–Zr liquidus projection (this work) based on [23,42,48,50]; (d) Cr–Nb–Zr solidus projection from Savel'yeva et Grum-Grzmaylo [50].

Figure 07 – Liquidus projection of the Cr–Hf–Nb system proposed in this work.

Figure 08 – Isothermal section at 1200 ºC of the Cr–Hf–Nb system proposed in this work.

Figure 09 – Micrographs (SEM/BSE) of as-cast Cr–Hf–Nb alloys (at.% / wt.%): (a) $Cr_{78}Hf_{19}Nb_{03}$ ($Cr_{52.5}Hf_{43.9}Nb_{3.6}$) (01AC); (b) $Cr_{83}Hf_{09}Nb_{08}$ ($Cr_{64.8}Hf_{24.1}Nb_{11.1}$) (02AC); (c) $Cr_{77}Hf_{09}Nb_{14}$ ($Cr_{57.9}Hf_{23.3}Nb_{18.8}$) (03AC); (d) $Cr_{71}Hf_{04}Nb_{25}$ ($Cr_{54.9}Hf_{10.6}Nb_{34.5}$) (04AC).

Figure 10 – X-ray diffractograms of as-cast Cr–Hf–Nb alloys (at.% / wt.%): (a) $Cr_{78}Hf_{19}Nb_{03}$ ($Cr_{52.5}Hf_{43.9}Nb_{3.6}$) (01AC); (b) $Cr_{83}Hf_{09}Nb_{08}$ ($Cr_{64.8}Hf_{24.1}Nb_{11.1}$) (02AC); (c) $Cr_{77}Hf_{09}Nb_{14}$ ($Cr_{57.9}Hf_{23.3}Nb_{18.8}$) (03AC); (d) $Cr_{71}Hf_{04}Nb_{25}$ ($Cr_{54.9}Hf_{10.6}Nb_{34.5}$) (04AC).

Figure 11 – Micrographs (SEM/BSE) of as-cast Cr–Hf–Nb alloys (at.% / wt.%): (a) $Cr_{58}Hf_{12}Nb_{30}$ ($Cr_{38.0}Hf_{26.9}Nb_{35.1}$) (05AC); (b) $Cr_{61}Hf_{2.5}Nb_{36.5}$ ($Cr_{45.2}Hf_{6.4}Nb_{48.4}$) (06AC); (c) $Cr_{35}Hf_{60}Nb_{05}$ ($Cr_{14.0}Hf_{82.4}Nb_{3.6}$) (07AC); (d) $Cr_{05}Hf_{90}Nb_{05}$ ($Cr_{1.5}Hf_{95.7}Nb_{2.8}$) (08AC).

Figure 12 – X-ray diffractograms of as-cast Cr–Hf–Nb alloys (at.% / wt.%): (a) $Cr_{58}Hf_{12}Nb_{30}$ ($Cr_{38.0}Hf_{26.9}Nb_{35.1}$) (05AC); (b) $Cr_{61}Hf_{2.5}Nb_{36.5}$ ($Cr_{45.2}Hf_{6.4}Nb_{48.4}$) (06AC); (c) $Cr_{35}Hf_{60}Nb_{05}$ ($Cr_{14.0}Hf_{82.4}Nb_{3.6}$) (07AC); (d) $Cr_{05}Hf_{90}Nb_{05}$ ($Cr_{1.5}Hf_{95.7}Nb_{2.8}$) (08AC).

Figure 13 – Micrographs (SEM/BSE) of heat-treated Cr–Hf–Nb alloys (at.% / wt.%): (a) $Cr_{78}Hf_{19}Nb_{03}$ ($Cr_{52.5}Hf_{43.9}Nb_{3.6}$) (01HT); (b) $Cr_{83}Hf_{09}Nb_{08}$ ($Cr_{64.8}Hf_{24.1}Nb_{11.1}$) (02HT); (c) $Cr_{77}Hf_{09}Nb_{14}$ ($Cr_{57.9}Hf_{23.3}Nb_{18.8}$) (03HT); (d) $Cr_{71}Hf_{04}Nb_{25}$ ($Cr_{54.9}Hf_{10.6}Nb_{34.5}$) (04HT).

Figure 14 – X-ray diffractograms of heat-treated Cr–Hf–Nb alloys (at.% / wt.%): (a) $Cr_{78}Hf_{19}Nb_{03}$ ($Cr_{52.5}Hf_{43.9}Nb_{3.6}$) (01HT); (b) $Cr_{83}Hf_{09}Nb_{08}$ ($Cr_{64.8}Hf_{24.1}Nb_{11.1}$) (02HT); (c) $Cr_{77}Hf_{09}Nb_{14}$ ($Cr_{57.9}Hf_{23.3}Nb_{18.8}$) (03HT); (d) $Cr_{71}Hf_{04}Nb_{25}$ ($Cr_{54.9}Hf_{10.6}Nb_{34.5}$) (04HT).

Figure 15 – Micrographs (SEM/BSE) of heat-treated Cr–Hf–Nb alloys (at.% / wt.%): (a) $Cr_{58}Hf_{12}Nb_{30}$ ($Cr_{38.0}Hf_{26.9}Nb_{35.1}$) (05HT); (b) $Cr_{61}Hf_{2.5}Nb_{36.5}$ ($Cr_{45.2}Hf_{6.4}Nb_{48.4}$) (06HT); (c) $Cr_{35}Hf_{60}Nb_{05}$ ($Cr_{14.0}Hf_{82.4}Nb_{3.6}$) (07HT); (d) $Cr_{05}Hf_{90}Nb_{05}$ ($Cr_{1.5}Hf_{95.7}Nb_{2.8}$) (08HT).

Figure 16 – X-ray diffractograms of heat-treated Cr–Hf–Nb alloys (at.% / wt.%): (a) $Cr_{58}Hf_{12}Nb_{30}$ ($Cr_{38.0}Hf_{26.9}Nb_{35.1}$) (05HT); (b) $Cr_{61}Hf_{2.5}Nb_{36.5}$ ($Cr_{45.2}Hf_{6.4}Nb_{48.4}$) (06HT); (c) $Cr_{35}Hf_{60}Nb_{05}$ ($Cr_{14.0}Hf_{82.4}Nb_{3.6}$) (07HT); (d) $Cr_{05}Hf_{90}Nb_{05}$ ($Cr_{1.5}Hf_{95.7}Nb_{2.8}$) (08HT).

Tables

Table 01 – Crystallographic data of the solid phases in the Cr–Hf, Cr–Nb and Hf–Nb binary systems.

Phase	Prototype	Space group	Pearson symbol	Wyckhoff position	Atom	*x*	*y*	*z*	*Cell Parameters* (Å)			Ref.
									a	*b*	*c*	
(Nb)	W	*Im*-3*m* 229	*cI2*	2*a*	Nb	0	0	0	3.3067	-	-	[61]
									3.3300	-	-	[62]
									3.2620	-	-	[63]
(Cr)	W	*Im*-3*m* 229	*cI2*	2*a*	Cr	0	0	0	2.8847	-	-	[61]
									2.8880	-	-	[65]
									2.8850	-	-	[64]
(Hf)-ht	W	*Im*-3*m* *229*	*cI2*	2*a*	Hf	0	0	0	3.6250			[66]
(Hf)-rt	Mg	$P6_3/mmc$ 194	*hP2*	2*c*	Hf	0.3333	0.6667	0.25	3.1965	-	5.0580	[67]
Cr_2Hf-ht *C*14	$MgZn_2$	$P6_3/mmc$ 194	*hP12*	2*a*	Cr	0	0	0	5.0670	-	8.2370	[68]
				4*f*	Hf	0.3333	0.6667	0.0570	5.0560	-	8.2100	[69]
				6*h*	Cr	0.8290	0.6580	0.2500	5.0800	-	8.2200	[70]
Cr_2Hf-rt *C*15	$MgCu_2$	*Fd*-3*m* 227	*cF*24	8*a*	Cr	0	0	0	7.1400	-	-	[71]
				16*d*	Hf	0.6250	0.6250	0.6250	7.0250	-	-	[72]
									7.1600	-	-	[73]
Cr_2Nb *C*15	$MgCu_2$	*Fd*-3*m* 227	*cF*24	8*a*	Cr	0	0	0	6.9910	-	-	[74]
				16*d*	Nb	0.6250	0.6250	0.6250	6.9500	-	-	[75]
									6.9740	-	-	[76]
									7.0740	-	-	[18]
(Hf,Nb)-ht	W	*Im*-3*m* 229	*cI2*	2*a*	Nb	0	0	0	3.44			[77]

Table 02 – Alloys prepared in the present work along with the phases identified (XRD) and the invariant reactions observed in the as-cast state.

Alloy Nr	Alloy Composition (at.% / wt.%)[1]	Observed phases in XRD[2]	Volume %[3]	Determined parameter cell[3] *a*	*b*	*c*	Observed reactions in solidification path
01	$Cr_{78}Hf_{19}Nb_{03}$	*C*14[4]	86	5.0618	-	8.2231	L ↔ *C*14
	($Cr_{52.5}Hf_{43.9}Nb_{3.6}$)	(Cr)	13	2.9206	-	-	L ↔ (Cr) + *C*14 (**e1-II1**)
		*C*15	1	7.1602	-	-	L + *C*14 ↔ (Cr) + *C*15 (**II1**)
02	$Cr_{83}Hf_{09}Nb_{08}$	*C*14[4]	32	5.0353	-	8.2323	L ↔ *C*14
	($Cr_{64.8}Hf_{24.1}Nb_{11.1}$)	(Cr)	62	2.9112	-	-	L ↔ (Cr) + *C*14 (**e1-II1**)
		*C*15	6	7.0180	-	-	L + *C*14 ↔ (Cr) + *C*15 (**II1**)
03	$Cr_{77}Hf_{09}Nb_{14}$	*C*14[4]	22	5.0785	-	8.0530	L ↔ *C*14
	($Cr_{57.9}Hf_{23.3}Nb_{18.8}$)	(Cr)	47	2.9164	-	-	L ↔ (Cr) + *C*14 (**e1-II1**)
		*C*15	31	7.0204	-	-	L + *C*14 ↔ (Cr) + *C*15 (**II1**)
04	$Cr_{71}Hf_{04}Nb_{25}$	*C*14[4]	2	5.0647	-	8.2405	L ↔ *C*14
	($Cr_{54.9}Hf_{10.6}Nb_{34.5}$)	(Cr)	27	2.9117	-	-	L + *C*14 ↔ *C*15 (**m-II1**)
		*C*15	71	6.9873	-	-	L + *C*14 ↔ (Cr) + *C*15 (**II1**)
							L ↔ (Cr) + *C*15 (**II1-e1**)
05	$Cr_{58}Hf_{12}Nb_{30}$	*C*14[4]	64	5.0937	-	8.1629	L ↔ *C*14
	($Cr_{38.0}Hf_{26.9}Nb_{35.1}$)	(Hf,Nb)-ht	7	3.3016	-	-	L + *C*14 ↔ *C*15 (**m-II2**)
		*C*15	29	6.9910	-	-	L + *C*15 ↔ (Hf,Nb)-ht + *C*14 (**II2**)
							L ↔ (Hf,Nb)-ht + *C*14 (**II2-e2**)
06	$Cr_{61}Hf_{2.5}Nb_{36.5}$	*C*14[4]	27	4.9385	-	8.0764	L ↔ *C*14
	($Cr_{45.2}Hf_{6.4}Nb_{48.4}$)	(Hf,Nb)-ht	6	3.6121	-	-	L + *C*14 ↔ *C*15 (**m-II2**)
		*C*15	67	6.9890	-	-	L + *C*15 ↔ (Hf,Nb)-ht + *C*14 (**II2**)
							L ↔ (Hf,Nb)-ht + *C*14 (**II2-e2**)
07	$Cr_{35}Hf_{60}Nb_{05}$	*C*14[4]	56	5.0882	-	8.2769	L ↔ *C*14
	($Cr_{14.0}Hf_{82.4}Nb_{3.6}$)	(Hf,Nb)-ht	5	3.5482	-	-	L ↔ (Hf,Nb)-ht + *C*14 (**II2-e2**)
		(Hf,Nb)-rt	39	3.1902	-	5.0455	(Hf,Nb)-ht ↔ (Hf,Nb)-rt + *C*14[5]
08	$Cr_{05}Hf_{90}Nb_{05}$	(Hf,Nb)-ht[4]	40	3.5657	-	-	L ↔ (Hf,Nb)-ht
	($Cr_{1.5}Hf_{95.7}Nb_{2.8}$)	(Hf,Nb)-rt	60	3.1918	-	5.0500	(Hf,Nb)-ht ↔ (Hf,Nb)-rt
09	$Cr_{07}Hf_{03}Nb_{90}$	(Hf,Nb)-ht[4]	100	3.2982	-	-	L ↔ (Hf,Nb)-ht
	($Cr_{3.9}Hf_{5.8}Nb_{90.3}$)						

1 – Atomic weight: Cr 51,9961, Hf 178,492, Nb 92,90638; 2 – Match prototype based on Table 1; 3 – Calculated by Rietveld refinement method (+/- 1 %); 4 – Observed primary precipitate phase; 5 – last regions to solidify.

Table 03 – Alloys prepared in the present work along with the phases identified (XRD) and the phase compositions (EPMA) observed in the heat-treated condition.

Alloy Nr	Alloy Composition (at.% / wt.%)[1]	Observed phases from XRD[2] (vol.%)[3]	Determined cell parameter[3] a	b	c	Phase equilibria field	Phase composition (at.% / wt.%)[1,4]
01	$Cr_{78}Hf_{19}Nb_{03}$	(Cr) (39)	2.9136	-	-	(Cr)	$Cr_{99.4}Hf_{0.5}Nb_{0.1}$ ($Cr_{98.1}Hf_{1.7}Nb_{0.2}$)
	($Cr_{52.5}Hf_{43.9}Nb_{3.6}$)	*C*15 (52)	7.1287	-	-	(*C*15)	$Cr_{70.0}Hf_{26.3}Nb_{3.7}$ ($Cr_{41.9}Hf_{54.1}Nb_{4.0}$)
		*C*14 (9)	5.0332	-	8.2240		-
02	$Cr_{83}Hf_{09}Nb_{08}$	(Cr) (46)	2.9101	-	-	(Cr)	$Cr_{98.2}Hf_{0.4}Nb_{1.4}$ ($Cr_{96.2}Hf_{1.4}Nb_{2.4}$)
	($Cr_{64.8}Hf_{24.1}Nb_{11.1}$)	*C*15 (48)	7.0625	-	-	(*C*15)	$Cr_{68.7}Hf_{17.2}Nb_{14.1}$ ($Cr_{44.9}Hf_{38.6}Nb_{16.5}$)
		*C*14 (6)	5.0515	-	8.2303		-
03	$Cr_{77}Hf_{09}Nb_{14}$	(Cr) (12)	2.9110	-	-	(Cr)	$Cr_{98.5}Hf_{0.4}Nb_{1.1}$ ($Cr_{96.7}Hf_{1.4}Nb_{1.9}$)
	($Cr_{57.9}Hf_{23.3}Nb_{18.8}$)	*C*15 (86)	7.0289	-	-	(*C*15)	$Cr_{68.5}Hf_{13.1}Nb_{18.4}$ ($Cr_{46.8}Hf_{30.7}Nb_{22.5}$)
		*C*14 (2)	5.0582	-	8.2469		-
04	$Cr_{71}Hf_{04}Nb_{25}$	(Cr) (7)	2.9148	-	-	(Cr)	$Cr_{99.0}Hf_{0.5}Nb_{0.5}$ ($Cr_{97.4}Hf_{1.7}Nb_{0.9}$)
	($Cr_{54.9}Hf_{10.6}Nb_{34.5}$)	*C*15 (92)	7.0073	-	-	(*C*15)	$Cr_{67.9}Hf_{4.4}Nb_{27.7}$ ($Cr_{51.2}Hf_{11.4}Nb_{37.4}$)
		*C*14 (1)	5.0619	-	8.2383		-
05	$Cr_{58}Hf_{12}Nb_{30}$	(Hf,Nb)-ht (10)	3.3148	-	-	(Hf,Nb)-ht	$Cr_{11.5}Hf_{5.5}Nb_{83.0}$ ($Cr_{6.4}Hf_{10.6}Nb_{83.0}$)
	($Cr_{38.0}Hf_{26.9}Nb_{35.1}$)	*C*15 (86)	7.1190	-	-	(*C*15)	$Cr_{63.6}Hf_{11.9}Nb_{24.5}$ ($Cr_{42.9}Hf_{27.6}Nb_{29.5}$)
		*C*14 (4)	5.1353	-	8.2494		-
06	$Cr_{61}Hf_{2.5}Nb_{36.5}$	(Hf,Nb)-ht (7)	3.2977	-	-	(Hf,Nb)-ht	$Cr_{13.0}Hf_{1.4}Nb_{85.6}$ ($Cr_{7.6}Hf_{2.8}Nb_{89.6}$)
	($Cr_{45.2}Hf_{6.4}Nb_{48.4}$)	*C*15 (93)	7.0111	-	-	(*C*15)	$Cr_{64.4}Hf_{2.5}Nb_{33.1}$ ($Cr_{48.7}Hf_{6.5}Nb_{44.8}$)
07	$Cr_{35}Hf_{60}Nb_{05}$	(Hf,Nb)-rt (23)	3.1928	-	5.1357	(Hf,Nb)-rt	$Cr_{1.7}Hf_{95.7}Nb_{2.6}$ ($Cr_{0.5}Hf_{98.1}Nb_{1.4}$)
	($Cr_{14.0}Hf_{82.4}Nb_{3.6}$)	*C*15 (77)	7.1655	-	-	(*C*15)	$Cr_{61.4}Hf_{32.2}Nb_{6.4}$ ($Cr_{33.5}Hf_{60.3}Nb_{6.2}$)
08	$Cr_{05}Hf_{90}Nb_{05}$	(Hf,Nb)-ht (37)	3.5822	-	-	(Hf,Nb)-ht	$Cr_{5.3}Hf_{78.6}Nb_{16.1}$ ($Cr_{1.7}Hf_{88.8}Nb_{9.5}$)
	($Cr_{1.5}Hf_{95.7}Nb_{2.8}$)	*C*15 (23)	7.1355	-	-	(*C*15)	$Cr_{61.2}Hf_{32.1}Nb_{6.7}$ ($Cr_{33.4}Hf_{60.1}Nb_{6.5}$)
		(Hf,Nb)-rt (40)	3.2143	-	5.0527	(Hf,Nb)-rt	$Cr_{1.9}Hf_{95.3}Nb_{2.8}$ ($Cr_{0.6}Hf_{97.9}Nb_{1.5}$)
09	$Cr_{07}Hf_{03}Nb_{90}$	(Hf,Nb)-ht	3.3022	-	-	(Hf,Nb)-ht	$Cr_{4.8}Hf_{3.9}Nb_{91.3}$ ($Cr_{2.7}Hf_{7.4}Nb_{89.9}$)
	($Cr_{3.9}Hf_{5.8}Nb_{90.3}$)	(100)					

1 – Atomic weight: Cr 51,9961, Hf 178,492, Nb 92,90638; 2 – Match prototype based on Table 1; 3 – calculated by Rietveld refinement method (+/- 1 %); 4 – EPMA (+/- 0.5 %).

Fig. 1

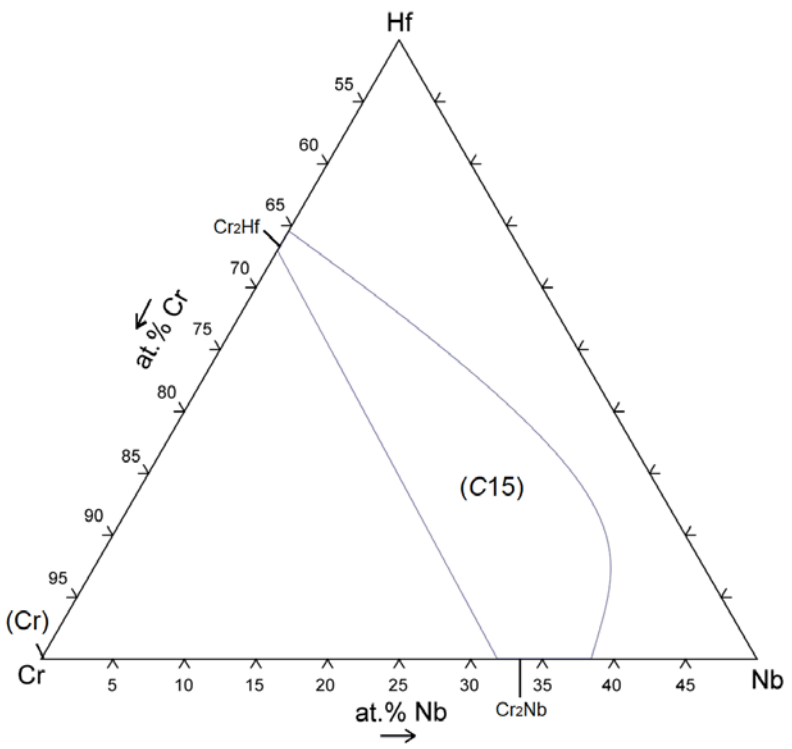
Hf
55
60
65
Cr2Hf
70
75
80
85
90
95
at.% Cr
(C15)
(Cr)
Cr
5
10
15
20
25
30
35
40
45
Nb
at.% Nb
Cr2Nb

Fig. 2

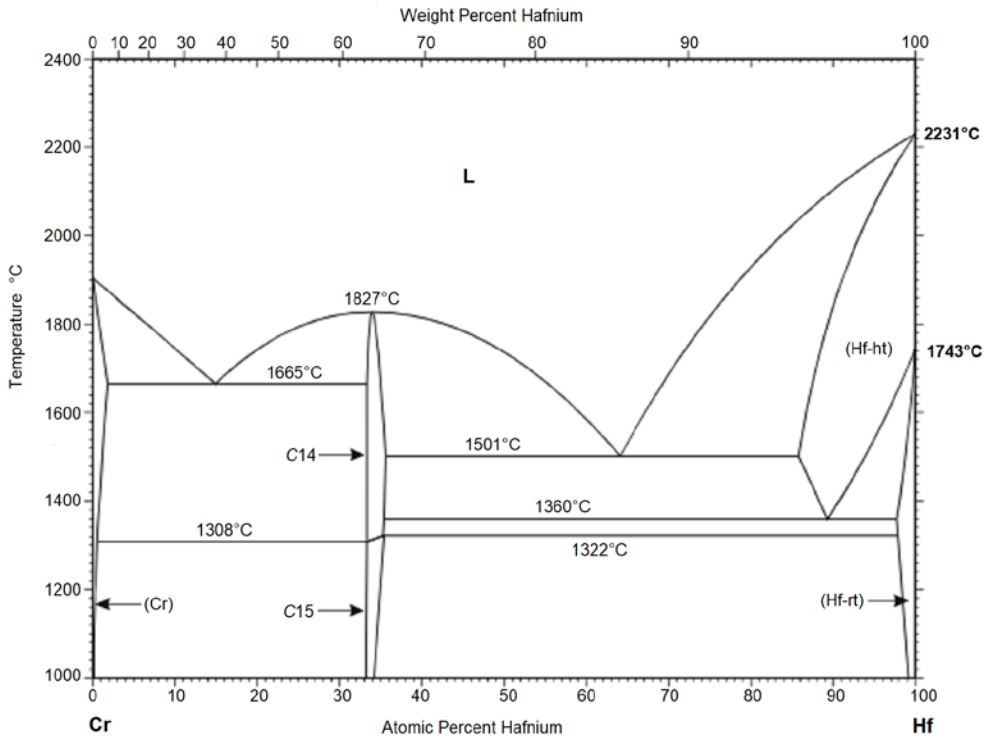
Weight Percent Hafnium
0 10 20 30 40 50 60 70 80 90 100
2400
2200
2000
1800
1600
1400
1200
1000
Temperature °C
L
2231°C
1827°C
1665°C
(Hf-ht)
1743°C
C14
1501°C
1360°C
1308°C
1322°C
(Cr)
C15
(Hf-rt)
0 10 20 30 40 50 60 70 80 90 100
Cr
Atomic Percent Hafnium
Hf

Fig. 3

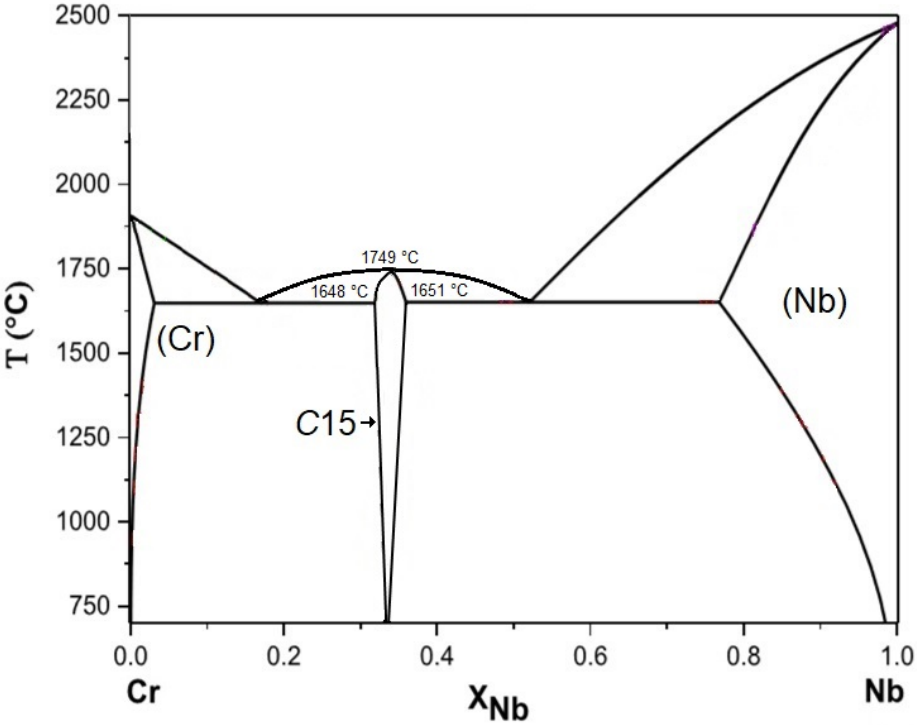
2500
2250
2000
1750
1500
1250
1000
750
T (°C)
1749 °C
1648 °C
1651 °C
(Cr)
C15→
(Nb)
0.0
0.2
0.4
0.6
0.8
1.0
Cr
x_{Nb}
Nb

Fig. 4

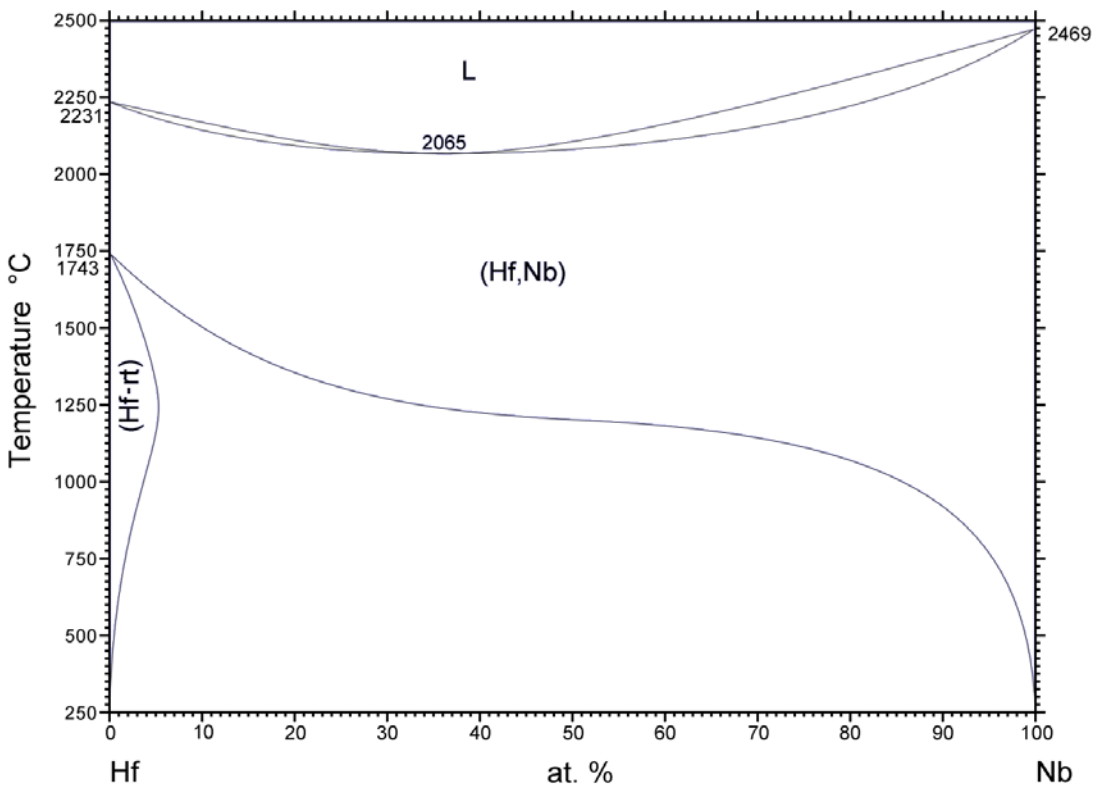
2500
2250
2231
2000
1750
1743
1500
1250
1000
750
500
250
Temperature °C
L
2469
2065
(Hf,Nb)
(Hf-rt)
0
10
20
30
40
50
60
70
80
90
100
Hf
at. %
Nb

Fig. 5

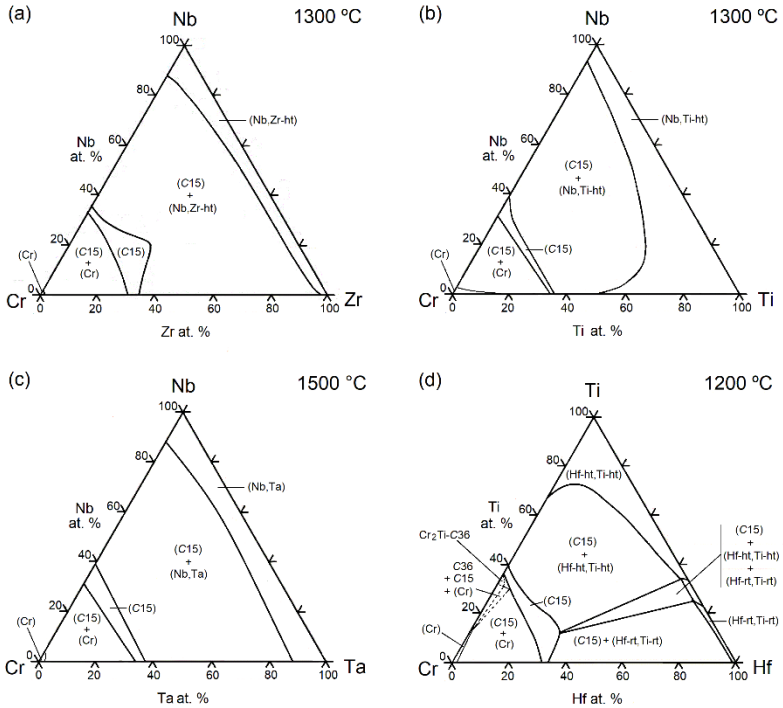
(a)
Nb
1300 °C
Nb at. %
(Nb,Zr-ht)
(C15) + (Nb,Zr-ht)
(C15) + (Cr)
(C15)
(Cr)
Cr
Zr
Zr at. %
(b)
Nb
1300 °C
Nb at. %
(Nb,Ti-ht)
(C15) + (Nb,Ti-ht)
(C15) + (Cr)
(C15)
(Cr)
Cr
Ti
Ti at. %
(c)
Nb
1500 °C
Nb at. %
(Nb,Ta)
(C15) + (Nb,Ta)
(C15) + (Cr)
(C15)
(Cr)
Cr
Ta
Ta at. %
(d)
Ti
1200 °C
Ti at. %
(Hf-ht,Ti-ht)
(C15) + (Hf-ht,Ti-ht)
Cr2Ti-C36
C36 + C15 + (Cr)
(C15) + (Hf-ht,Ti-ht) + (Hf-rt,Ti-rt)
(Hf-rt,Ti-rt)
(C15) + (Hf-rt,Ti-rt)
(C15) + (Cr)
(C15)
(Cr)
Cr
Hf
Hf at. %

Fig. 6

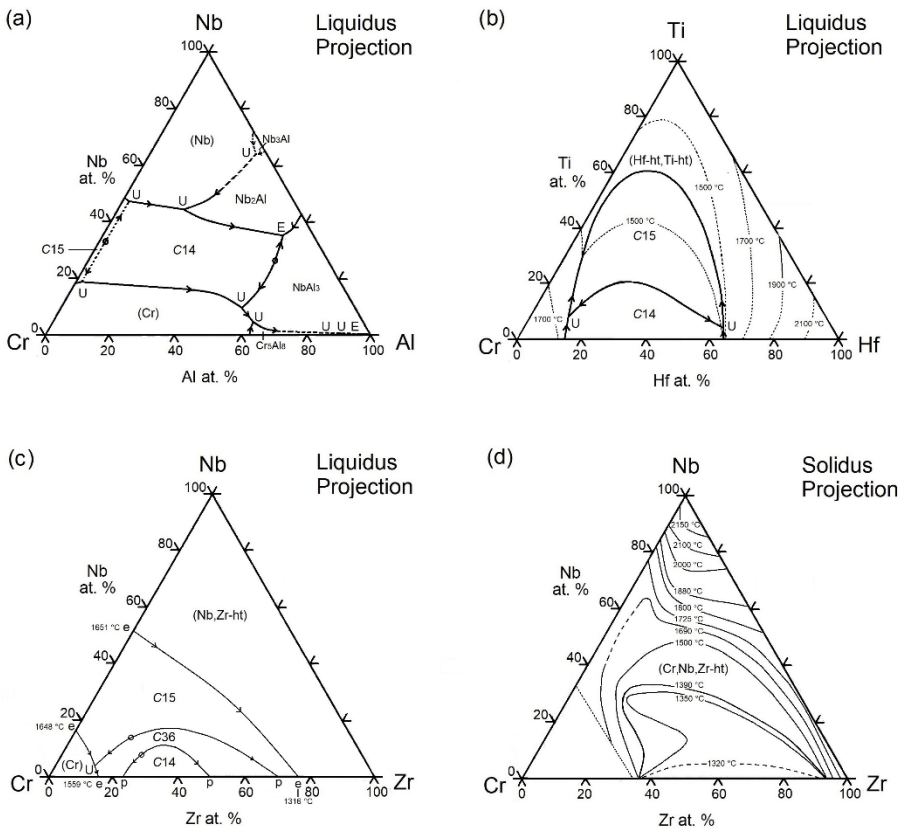
(a)
Nb
Liquidus Projection
Nb at. %
(Nb)
Nb3Al
Nb2Al
C15
C14
NbAl3
(Cr)
Cr5Al8
Cr
Al
Al at. %
(b)
Ti
Liquidus Projection
Ti at. %
(Hf-ht,Ti-ht)
C15
C14
Cr
Hf
Hf at. %
(c)
Nb
Liquidus Projection
Nb at. %
(Nb,Zr-ht)
C15
C36
C14
(Cr)
Cr
Zr
Zr at. %
(d)
Nb
Solidus Projection
Nb at. %
(Cr,Nb,Zr-ht)
Cr
Zr
Zr at. %

Fig. 7

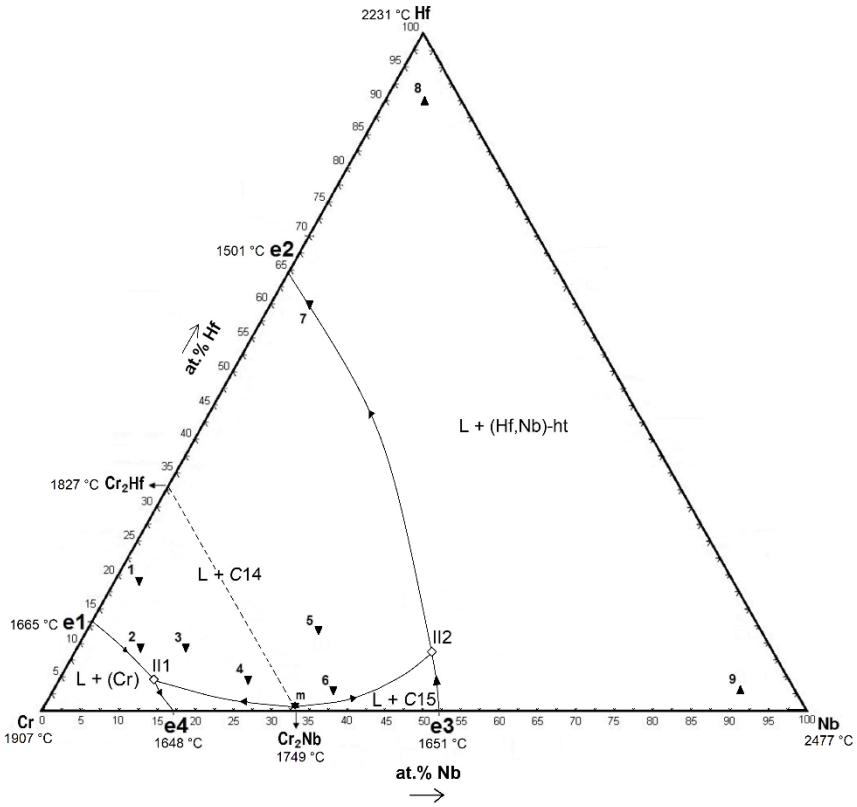
2231 °C Hf
1501 °C e2
1827 °C Cr2Hf
1665 °C e1
L + (Hf,Nb)-ht
L + C14
L + (Cr)
Il1
Il2
L + C15
Cr
1907 °C
e4
1648 °C
Cr2Nb
1749 °C
e3
1651 °C
Nb
2477 °C
at.% Hf
at.% Nb

Fig. 8

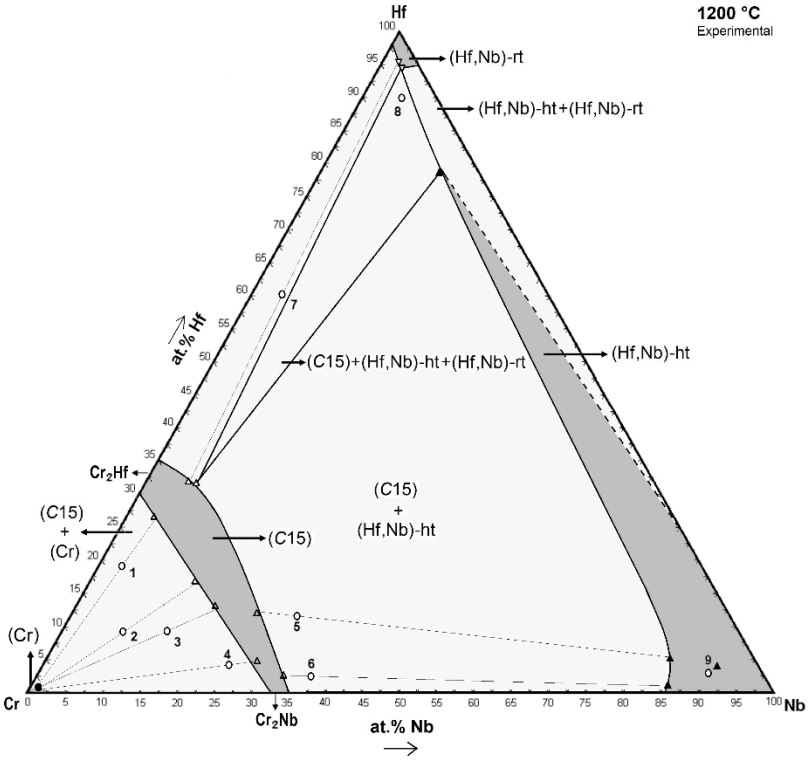
Hf
1200 °C
Experimental
(Hf,Nb)-rt
(Hf,Nb)-ht+(Hf,Nb)-rt
(C15)+(Hf,Nb)-ht+(Hf,Nb)-rt
(Hf,Nb)-ht
Cr2Hf
(C15)
+
(Cr)
(C15)
(C15)
+
(Hf,Nb)-ht
(Cr)
Cr
Cr2Nb
Nb
at.% Hf
at.% Nb

Fig. 9

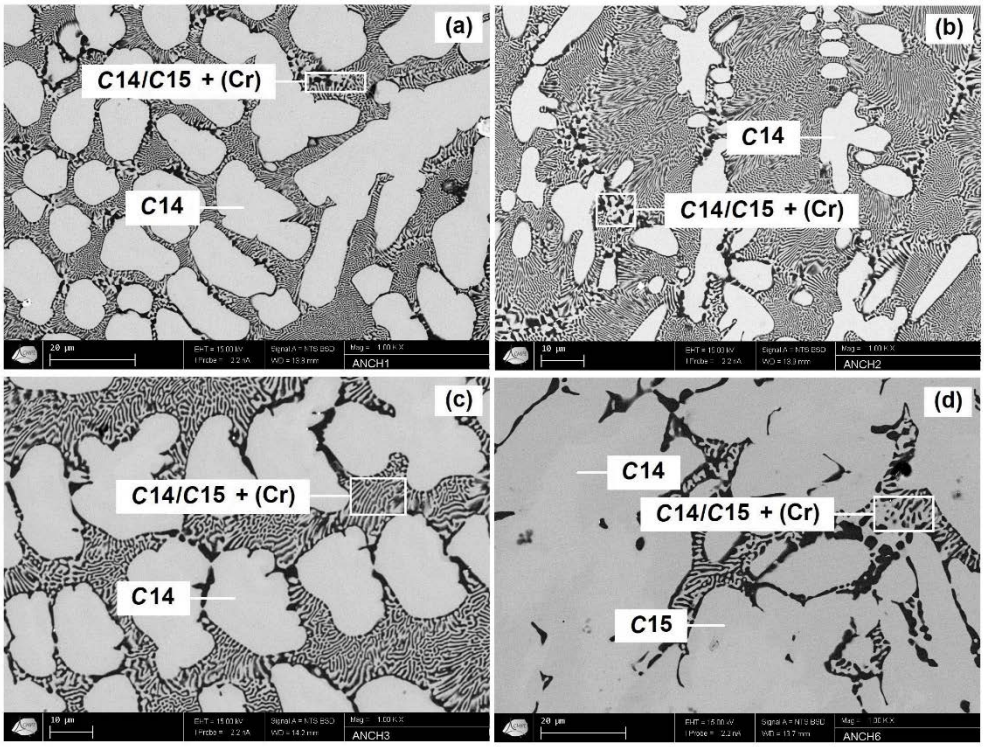
(a)
C14/C15 + (Cr)
C14
(b)
C14
C14/C15 + (Cr)
(c)
C14/C15 + (Cr)
C14
(d)
C14
C14/C15 + (Cr)
C15

Fig. 10

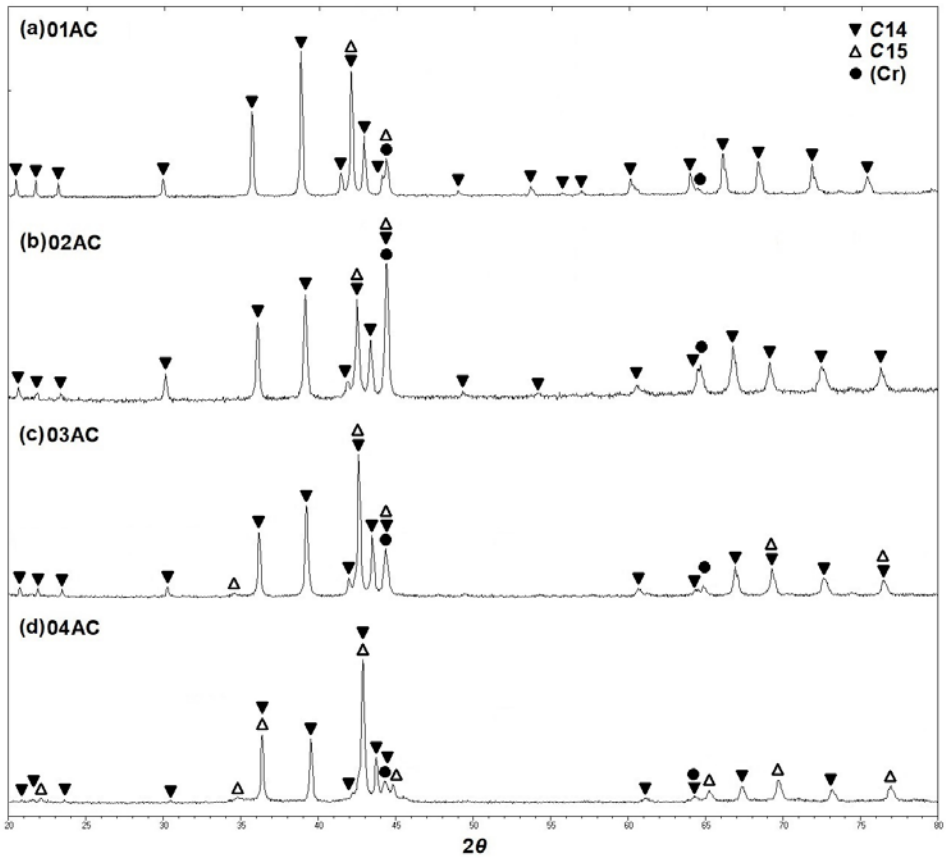
(a)01AC
(b)02AC
(c)03AC
(d)04AC
C14
C15
(Cr)
2θ

Fig. 11

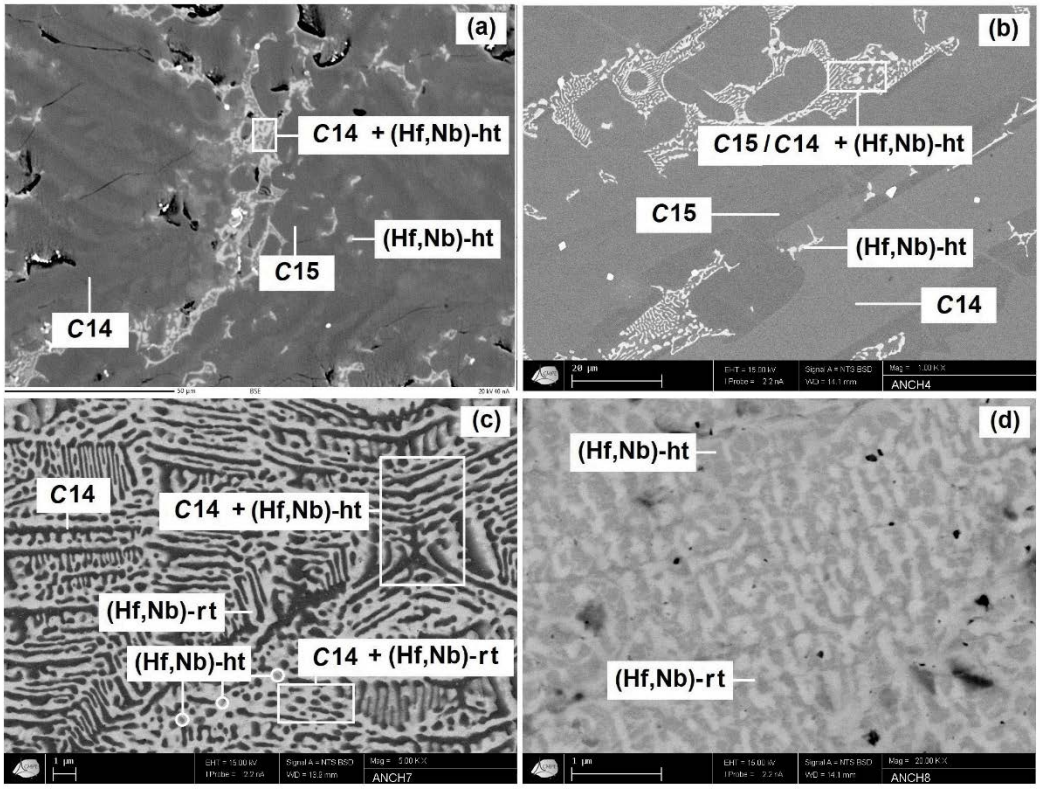
(a)
C14 + (Hf,Nb)-ht
(Hf,Nb)-ht
C15
C14
(b)
C15 / C14 + (Hf,Nb)-ht
C15
(Hf,Nb)-ht
C14
(c)
C14
C14 + (Hf,Nb)-ht
(Hf,Nb)-rt
(Hf,Nb)-ht
C14 + (Hf,Nb)-rt
(d)
(Hf,Nb)-ht
(Hf,Nb)-rt

Fig. 12

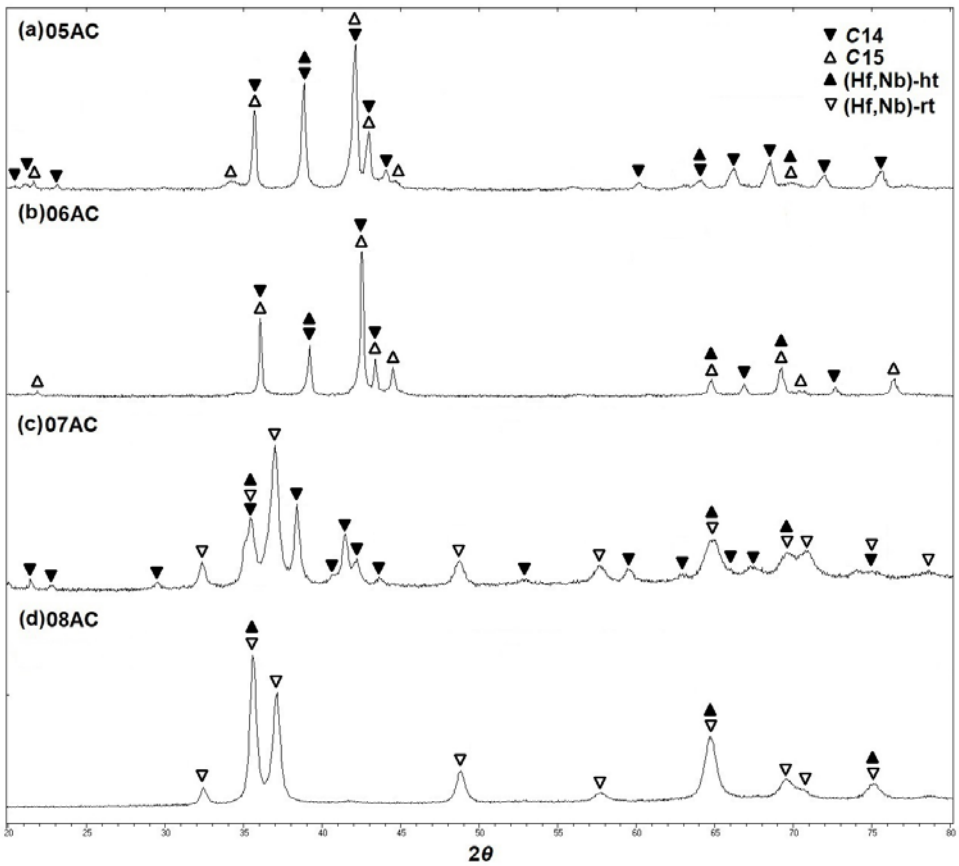
(a)05AC
(b)06AC
(c)07AC
(d)08AC
C14
C15
(Hf,Nb)-ht
(Hf,Nb)-rt
2θ

Fig. 13

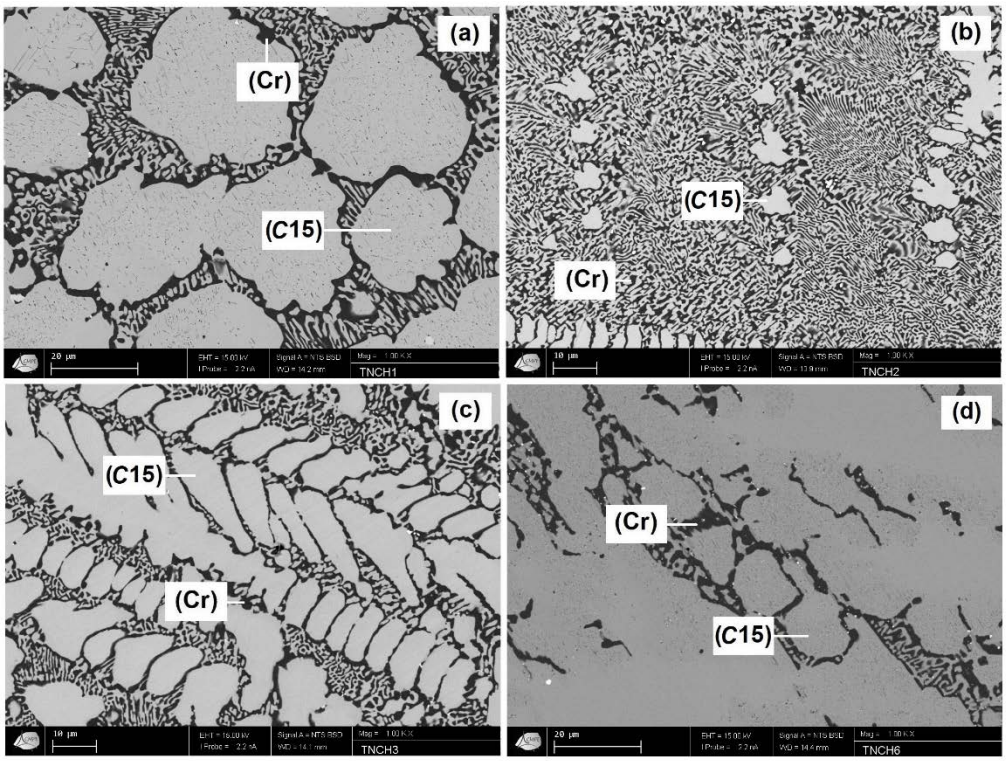
(a)
(Cr)
(C15)
(b)
(C15)
(Cr)
(c)
(C15)
(Cr)
(d)
(Cr)
(C15)

Fig. 14

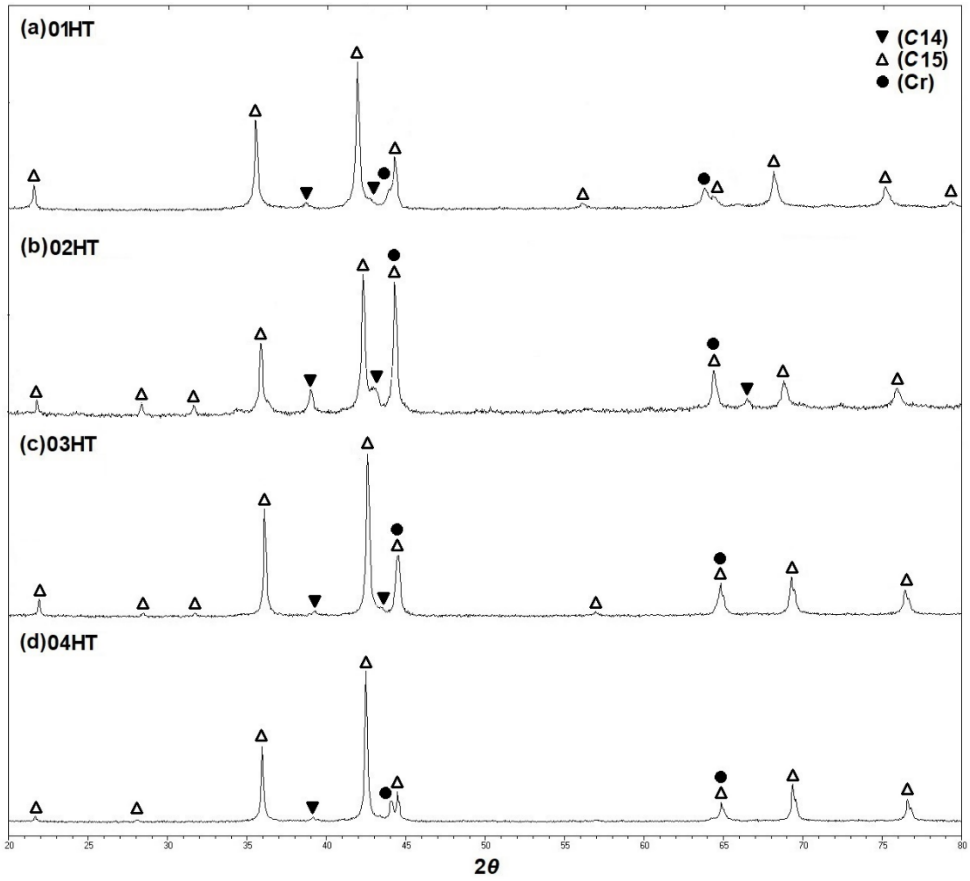
(a)01HT
(b)02HT
(c)03HT
(d)04HT
▼ (C14)
△ (C15)
● (Cr)
20
25
30
35
40
45
50
55
60
65
70
75
80
2θ

Fig. 15

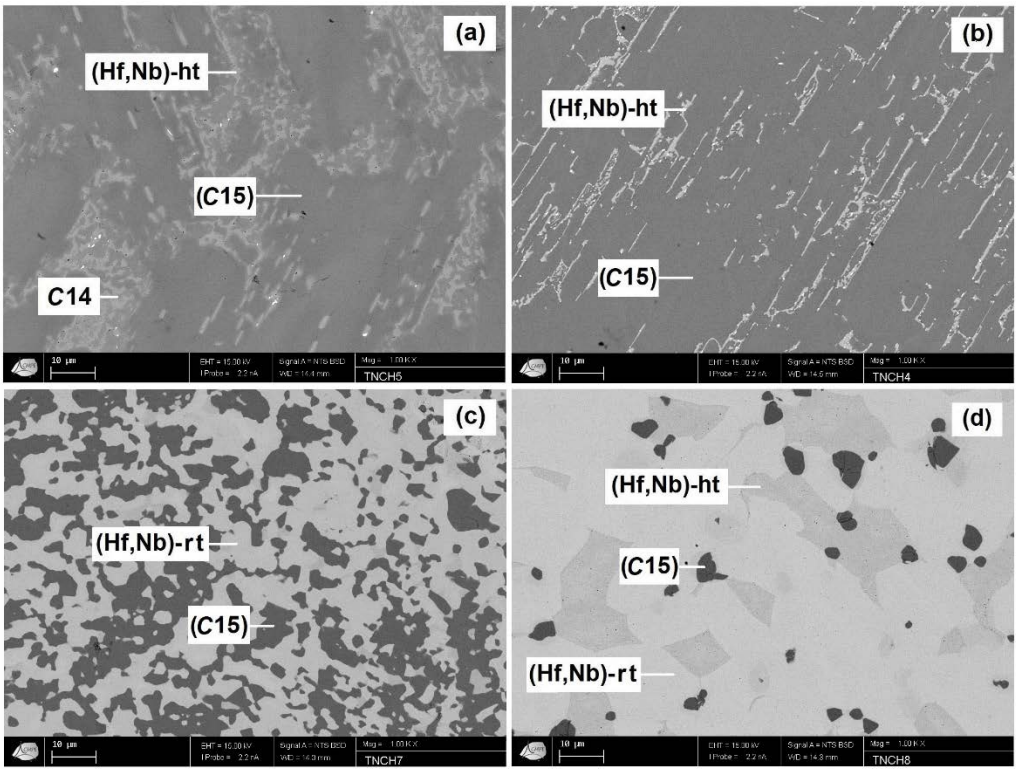
(a)
(Hf,Nb)-ht
(C15)
C14
(b)
(Hf,Nb)-ht
(C15)
(c)
(Hf,Nb)-rt
(C15)
(d)
(Hf,Nb)-ht
(C15)
(Hf,Nb)-rt

Fig.16

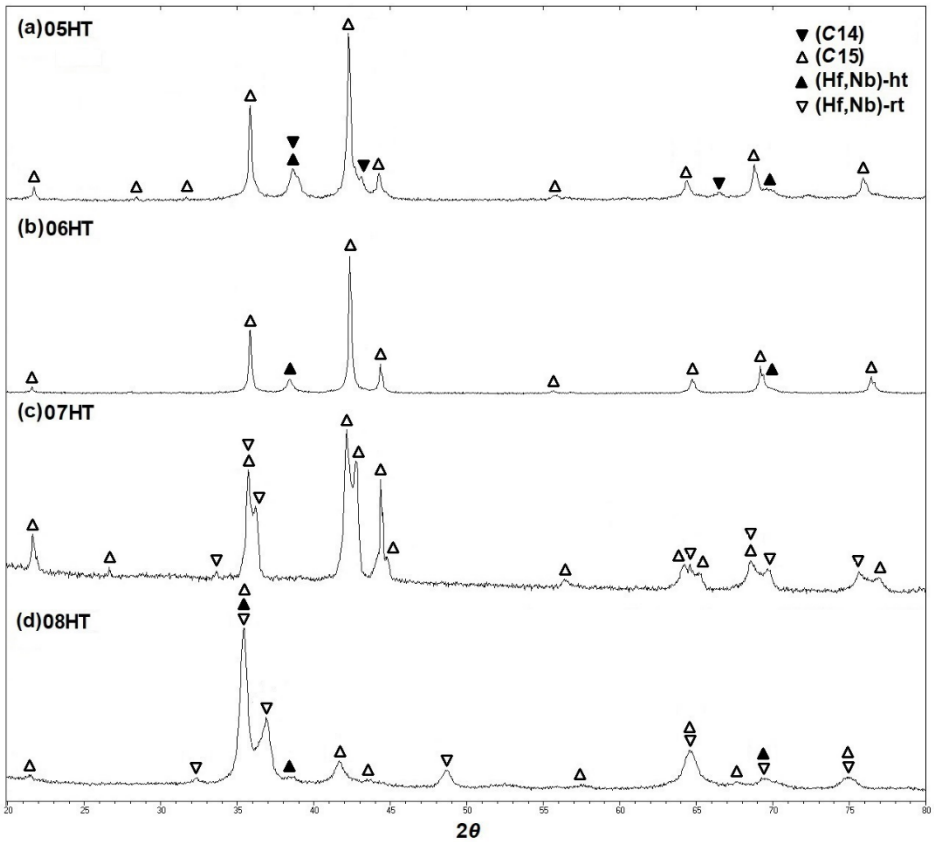
(a)05HT
(b)06HT
(c)07HT
(d)08HT
▼ (C14)
△ (C15)
▲ (Hf,Nb)-ht
▽ (Hf,Nb)-rt
2θ